Electrochemical Energy Reviews (2025) 8:11
https://doi.org/10.1007/s41918-025-00246-z

REVIEW ARTICLE

Recent Advances in Solid Oxide Electrolysis Cells for Solar Energy Conversion

Chen-Ge Chen[1] · Chenyu Xu[1] · Peng-Fei Sui[2] · Guangyu Deng[1] · Yi-Cheng Wang[2] · Jinhao Mei[1] · Entao Zhang[1] · Yanwei Zhang[1] · Jing-Li Luo[2]

Received: 23 September 2024 / Revised: 23 January 2025 / Accepted: 8 April 2025

Abstract

To implement global energy transitions, the efficient utilization of clean energy plays a central role in the process and has become an imperative task. Among various approaches, solid oxide electrolysis cells (SOECs) stand out as exceptional energy conversion devices because of their ability to transform thermal and electrical energy into chemical energy. For example, solar energy is a clean and renewable energy source and can be effectively harnessed to power SOECs, thereby facilitating efficient conversion from solar to chemical energy. In light of the growing interest in leveraging SOECs for solar energy conversion, a systematic collation and comprehensive review of the relevant studies reported thus far have yet to be conducted. This review summarizes and analyzes recent advances in the field of SOECs, including their fundamentals, performance metrics, current status, and methods of integration with solar energy. It also proposes various optimization strategies for the existing integration of solar energy with SOEC systems, with a specific emphasis on full-spectrum utilization. Finally, this study provides a perspective on the future development and challenges for SOECs in the context of solar energy conversion.

Keywords SOEC · Solar energy · Energy efficiency · Energy conversion · Solar energy integration · Hydrogen

Abbreviations

SOECs	Solid oxide electrolysis cells
PEMECs	Proton exchange membrane electrolysis cells
SOFCs	Solid oxide fuel cells
CSP	Concentrated solar power
O-SOECs	Oxygen-ion conducting solid oxide electrolysis cells
MIEC	Mixed ionic and electronic conducting
YSZ	Yttria-stabilized zirconia
FE	Faradaic efficiency
STF	Solar-to-fuel
STH	Solar-to-hydrogen
SOPCs	Solid oxide photoelectrolysis cells
AECs	Alkaline electrolysis electrolysis cells
AEMECs	Anion exchange membrane electrolysis cells
R-SOCs	Reversible solid oxide cells
TPB	Triple phase boundary
H-SOECs/PCECs	Protonic ceramic electrochemical cells
TCOs	Triple-conducting oxides
GDC	Gadolinia-doped ceria
SEC	Specific energy consumption
R-PCECs	Reversible protonic ceramic electrochemical cells
PETE	Photon-enhanced thermionic emission

✉ Chenyu Xu
mrxcy@zju.edu.cn

✉ Yanwei Zhang
zhangyw@zju.edu.cn

✉ Jing-Li Luo
jingli.luo@ualberta.ca

[1] State Key Laboratory of Clean Energy Utilization, Zhejiang University, Hangzhou 310027, Zhejiang, China

[2] Department of Chemical and Materials Engineering, University of Alberta, Edmonton, AB T6G 1H9, Canada

1 Introduction

With the ongoing transformation of energy systems and the scarcity of traditional energy sources, the quest for more suitable alternative energy sources is more critical than ever. In 2016, almost all the member states of the United Nations signed the Paris Agreement, which states that by the year 2100, the global average temperature increase must

Published online: 06 June 2025

be maintained well below 2 °C above pre-industrial levels, and efforts are required to limit the temperature increase even further to 1.5 °C [1, 2]. In response to the Paris Agreement, many countries are transitioning toward clean and low-carbon energy sources to promote the decarbonization of their economies [3]. To reduce carbon dioxide emissions [4], capturing and converting CO_2 [5–7], as well as developing clean fuel processes, have become important. As a result, an increasing number of researchers are turning their attention to the production of H_2 [8]. On the one hand, H_2 can be applied to convert CO_2 into fuels or higher-value chemicals [9–11], such as CH_4 and C_2H_4 [12–15]. On the other hand, H_2 is a pollution-free fuel; it only produces H_2O upon combustion, making it environmentally friendly [16].

Hydrogen can be directly produced from H_2O electrolysis. Currently, four main types of H_2O electrolysis cells are used in power-to-gas systems: alkaline electrolysis cells (AECs), proton exchange membrane electrolysis cells (PEMECs), anion exchange membrane electrolysis cells (AEMECs), and solid oxide electrolysis cells (SOECs). For decades, AECs have been widely used in industry for hydrogen production and are known for their stability and reliability, but their low current density may limit their efficiency and scalability [17]. The PEMECs operate via the conduction of protons through a proton exchange membrane [18] and can be coupled with renewable energy. The cost of platinum catalysts is the main factor that may restrict their economic viability in large-scale applications. The AEMECs operate through the conduction of hydroxide ions via an anion exchange membrane, allowing for the use of non-precious metal catalysts. They face challenges related to ion conductivity and long-term stability, such as the chemical degradation of membranes under high-pH conditions [19].

The SOECs operate at high temperatures by transporting ions (O^{2-}/H^+) through solid electrolytes and are currently in the pre-commercial stage of large-scale deployment. The SOECs are receiving significant attention because of their remarkable energy conversion efficiency, which can approach 100% [20–22]. When operating at temperatures above 500 °C, SOECs efficiently harness the input electrical power and waste thermal energy from other systems [23], thereby increasing the overall energy utilization efficiency. Moreover, SOECs boast multiple advantages, such as low electrode overpotential, no requirement for costly catalysts (e.g., platinum and ruthenium), and the ability to perform co-electrolysis using various energy carriers [24–26], including steam and carbon monoxide [27]. As the reverse reaction process of solid oxide fuel cells (SOFCs) [28, 29], SOEC technology can also be applied to reversible solid oxide cells (R-SOCs), enabling a single device to generate power in fuel cell mode or produce chemical energy carriers in electrolysis mode. This highlights the versatility and flexibility of SOECs in the field of energy conversion and storage. In this work, we focus mainly on the role of SOECs as devices for chemical energy conversion without extensively delving into their performance in R-SOCs. Owing to their high energy conversion efficiency, SOECs have the potential to utilize various hydrogen sources [30, 31], including biogas and industrial byproducts. The high efficiency and adaptability of SOEC technology to diverse hydrogen sources make it a strong contender for future hydrogen production [32, 33], especially in regions rich in renewable energy. Moreover, the use of renewable sources as energy inputs for SOECs further enhances the energy conversion process, making it cleaner, more efficient, and more sustainable.

Solar energy [34], recognized for its cleanliness and renewability, is an ideal energy source for SOECs. It can be coupled with SOECs to supply electricity through concentrated solar power (CSP) or photovoltaics [35], as well as to provide high-temperature heat through concentrated solar thermal systems. As illustrated in Fig. 1, the solar-driven electrolysis process not only achieves efficient conversion of solar energy to chemical energy but also contributes to building a sustainable energy system. Using solar energy for high-temperature steam electrolysis results in negligible carbon emissions, minimal environmental impact, and the generation of "green hydrogen" making this process highly environmentally friendly. The integration of SOEC technology with solar energy has the potential to achieve higher solar-to-hydrogen efficiency and holds promise for commercializing hydrogen production, thus making a significant contribution to the development of a hydrogen economy.

This study systematically elucidates recent advances from four critical perspectives: fundamentals, performance metrics, current status, and methods for integrating SOECs with solar energy. Through this comprehensive analysis, the study provides a scientific basis and strategic guidance for the application of SOECs in the field of clean energy, particularly in the context of solar energy utilization, and contributes to the pursuit of a cleaner and more sustainable energy future.

2 Fundamentals of SOECs

2.1 SOEC Structure

The SOECs are composed of three primary layers: the electrolyte, the cathode, and the anode. As illustrated in Fig. 2, a dense electrolyte layer is situated at the center, with the porous anode and cathode positioned on either side. The electrolyte separates the gases at the electrodes and facilitates the transport of ions, electrons, protons, and other particles during the reaction. The anode and cathode are designed to catalyze the chemical reactions of the reactants, with their porous structure promoting the diffusion and transport of reactants and products. Electrodes in SOECs are sometimes

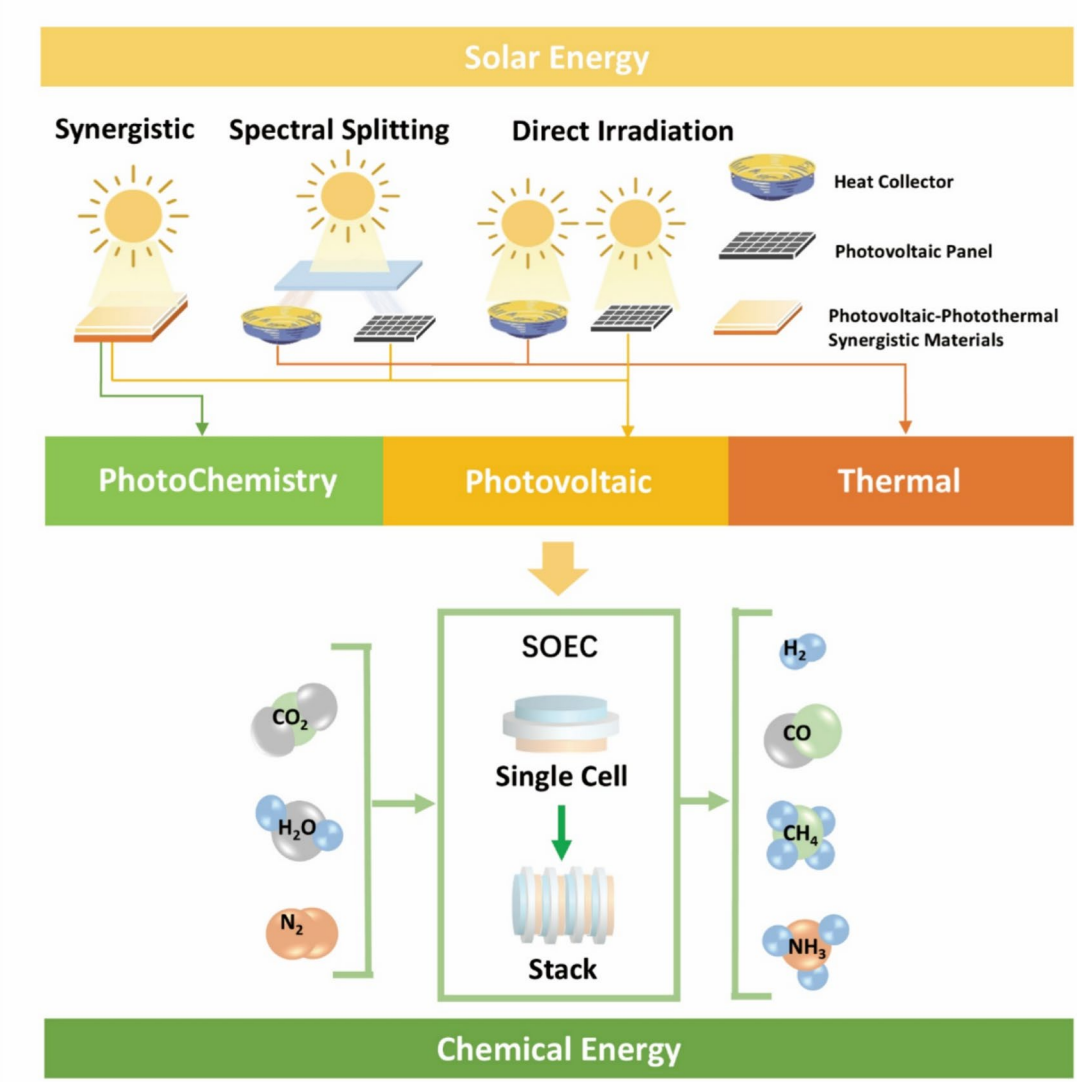

Fig. 1 SOECs for chemical reactions based on solar energy

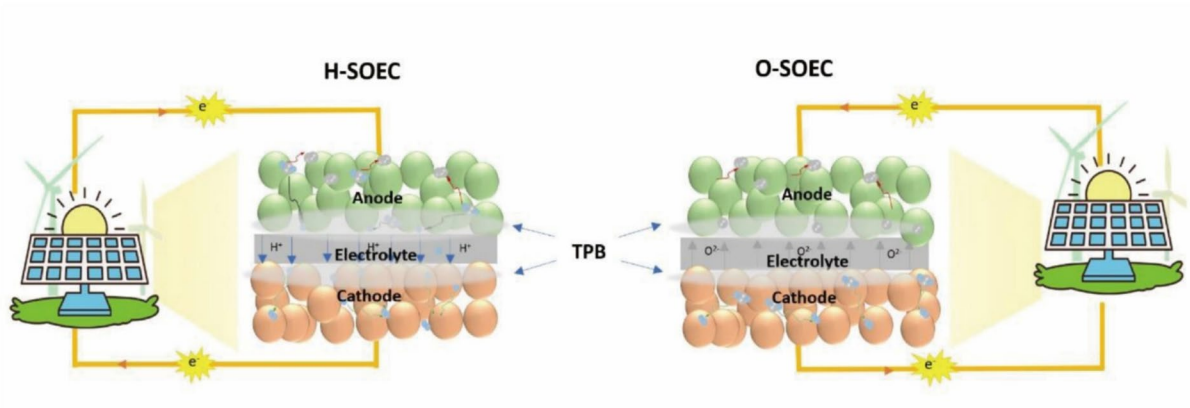

Fig. 2 The structure of the SOEC

distinguished as air or fuel electrodes; the air electrode is where O_2 is generated, and the fuel electrode is where fuels such as H_2 and CH_4 are produced.

Generally, an SOEC operates at relatively high temperatures, typically ranging from 500 to 1 000 °C. The specific temperature range that can be effectively utilized largely depends on the characteristics of the materials [36]. In operational mode, the fuel electrode is supplied with reactants. A defined electrolysis voltage is applied across the anode and cathode of the SOEC. Concurrently, on the air electrode side, an electrochemical reaction occurs at the triple phase boundary (TPB), where the gas, electronic conductor, and ionic conductor converge [22, 37]. Electrons are liberated at this TPB because of the electrochemical process. These electrons are subsequently conducted through an external circuit and ultimately reach the fuel electrode.

2.2 Mechanisms of Solar Energy Utilization in SOECs

To reduce the costs of electrical energy input, the integration of other forms of clean energy sources with SOECs to supply direct electrical or thermal energy is essential. Solar energy, with its abundance and renewable capacity, plays a pivotal role in SOEC industrialization [38]. The utilization of solar energy materializes in two primary forms, which are distinguished by their effects: thermal and nonthermal [39], as shown in Fig. 3. The nonthermal effect refers to the direct extraction and utilization of photoexcited charge carriers, such as conversion into electrical energy through photovoltaic panels or chemical reactions through catalysis [40, 41]. When light irradiates semiconductor or plasmonic materials, if the photon energy exceeds the bandgap energy of the material, then the light can excite electrons such that they transition from the valence band to the conduction band, creating electron–hole pairs [42]. These energetic charge carriers can participate in and drive chemical reactions. For plasmonic materials, such as metallic nanoparticles, when the frequency of incident photons matches the intrinsic frequency of surface electrons oscillating against the restoring force of positive nuclei, a resonant photoinduced collective oscillation of free electrons occurs, which is known as the surface plasmon resonance effect [39]. This effect dramatically enhances light absorption.

Conversely, the thermal effect involves the transfer of energy from energetic carriers to the lattice through phonon emission, thereby converting solar energy into thermal energy, or the direct absorption of photons by the lattice to generate thermal energy. In both semiconductor and plasmonic materials, radiative and/or nonradiative decay occurs shortly after the generation of energetic carriers. During radiative decay, energy is emitted in the form of photons, which can be measured via photoluminescence spectroscopy. Along with the nonradiative relaxation of energetic carriers, electron–phonon scattering occurs after electron–electron scattering, and the energy of the electrons is eventually dissipated as thermal energy. In simple terms, the energy of the carriers is transferred to phonons, thus intensifying the lattice vibrations, which macroscopically manifests as a temperature increase [39].

Typically, to enable an SOEC to exploit the nonthermal effects of solar energy, photovoltaic panels are integrated

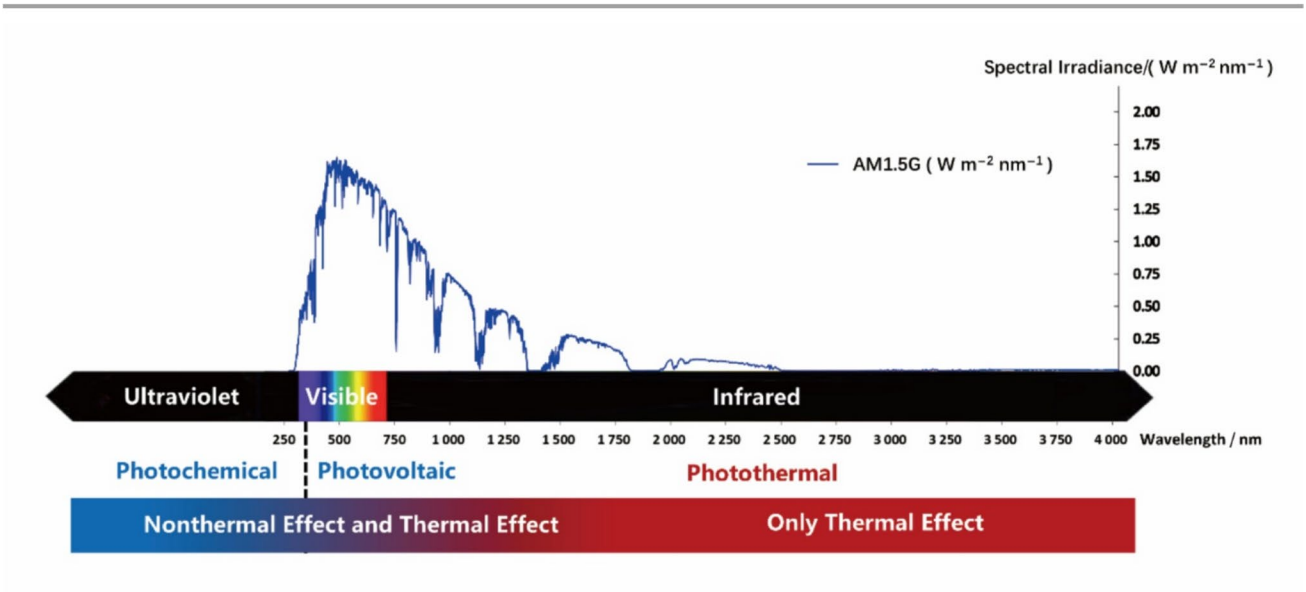

Fig. 3 Thermal and nonthermal effects of solar energy

to convert solar irradiation into electrical energy. Alternatively, heat collectors such as parabolic reflectors can be used to focus solar energy, thereby converting solar energy into thermal energy for input into the system.

2.3 Classification of Solid Electrolyte Types

Electrolyte materials are the most important components of SOECs. Based on the different transport mechanisms of electrolyte charge carriers, researchers have divided SOECs into two categories [43]. One category consists of SOECs that use oxygen ions (O^{2-}) as the transport medium, also known as oxygen-ion-conducting solid oxide electrolysis cells (O-SOECs). The other category consists of SOECs that use protons (H^+) as the transport medium, also known as protonic ceramic electrochemical cells (H-SOECs or PCECs) [44]. Researchers hope to introduce mixed ionic and electronic conducting (MIEC) materials to form triple-conducting oxides (TCOs) [45], thereby extending the TPB from the electrolyte/electrode interface to the interior of the SOEC [46]. This extension increases the number of reaction sites for water oxidation and oxygen reduction reactions [47]. In addition, the higher density of the TPB can provide more active areas to support reactions and rapidly promote the movement of O^{2-}/H^+ [48].

2.3.1 O-SOECs

The mechanism of an O-SOEC is shown in Fig. 2. At the cathode, water is adsorbed on the electrode surface through a reduction reaction and decomposes into H_2 and O^{2-}. Owing to the oxygen concentration gradient and potential difference, O^{2-} eventually reaches the anode surface, and O_2 is generated [49]. Currently, the most common electrolytes are those that conduct O^{2-}, which mainly include fluorite oxides (such as yttria-stabilized zirconia (YSZ) [50–52] and gadolinia-doped ceria (GDC)) and perovskite oxides (such as Mg/Sr-doped $LaGaO_3$ and Y-doped $BaZrO_3$) [37, 53]. Among them, YSZ, as a representative ion-conducting electrolyte, has been widely applied [54]. However, YSZ only has a high conductivity (0.01–0.1 S cm^{-1}) at high temperatures (800–1 000 °C) [36, 55, 56]. Operating at these temperatures is thermodynamically advantageous, as it can reduce the power demand for steam electrolysis, but such high operating temperatures can lead to several issues, such as poor long-term cell stability, interlayer diffusion, and material collapse [57].

2.3.2 H-SOECs

Owing to the problems caused by high temperatures, the development of SOECs that operate at medium temperatures (500–700 °C) has recently received widespread attention [58]. The mechanism of an H-SOEC is shown in Fig. 2. Water decomposes on the anode side, producing O_2 and H^+. The H^+ protons are then transported through the electrolyte to the cathode, where they combine with electrons to produce H_2. For H-SOECs, only pure hydrogen is produced on the hydrogen electrode side, eliminating the need for further gas separation. Moreover, the activation energy for proton conduction is significantly lower (0.4–0.6 eV) than that for ion conduction [59]. Therefore, H-SOECs can exhibit greater electrochemical performance at lower operating temperatures (450–650 °C) [60]. Currently, the materials that primarily conduct protons are barium-based perovskites [61], including $BaCe_{0.6}Zr_{0.3}Y_{0.1}O_{3-\delta}$ (BCZY) [62], $BaCe_{0.4}Zr_{0.4}Y_{0.1}Yb_{0.1}O_{3-\delta}$ (BCZYYb4411), $BaCe_{0.7}Zr_{0.1}Y_{0.1}Yb_{0.1}O_{3-\delta}$ (BCZYYb7111), and $BaZr_{0.8}Y_{0.2}O_{3-\delta}$ (BCY), all of which are used as electrolyte materials because of their high proton conductivity.

3 Performance Metrics for SOEC Systems

To obtain a profound understanding of how different types of SOEC systems perform when various energy sources are input and converted into chemical energy, and to better assess their viability, establishing evaluation metrics for the parameters and efficiency during SOEC operation is imperative. These metrics span several aspects, from thermodynamic performance and kinetic characteristics to long-term stability, to fully assess the SOEC performance.

3.1 Assessment of the SOEC Efficiency

Energy efficiency, also known as first-law efficiency [63], is defined as the ratio of the total useful output energy (usually calculated from the lower heating value (LHV) of the output products) to the total energy input. Therefore, the energy efficiency can be calculated via Eq. (1):

$$\eta_{en} = \frac{LHV \cdot N_{out}}{w_{tot}} \quad (1)$$

where N_{out} is the flow rate of the output gas (mol s^{-1}) and w_{tot} is the total energy input into the system, including the required thermal energy and electrical energy.

During H_2O electrolysis, electrical power is input into the SOEC and converted into the chemical energy of the products.

The electrolysis efficiency η_{ele},which is typically defined as the ratio of the LHV to the electrical energy consumed [64], can be calculated via Eq. (2):

$$\eta_{ele} = \frac{\sum_i \left(n_{i,out} - n_{i,in}\right)}{E_{input}} \tag{2}$$

$$E_{input} = V_{demand} \times J \tag{3}$$

where n_i is the flow flux of species i (mol s^{-1}). E_{input} is the electrical power consumed by electrolysis, which can be calculated via Eq. (3) by multiplying the demanded voltage for electrolysis V_{demand} by the operating current density J.

The faradaic efficiency (FE) is considered an important indicator of electrochemical devices [21, 65]. It is usually defined as the ratio of the actual output to the theoretical output. For SOECs, the FE can be used to reflect the electron utilization rate in the electrocatalytic reaction process and is an important parameter for assessing the practical value of the SOEC. The FE can be calculated via Eq. (4):

$$FE = \frac{n_{H_2}}{2F} \tag{4}$$

where n_{H_2} is the flow rate of H_2 (mol s^{-1}) and F is the Faraday constant (96 485 C mol^{-1}).

To analyze the performance of an SOEC under different operating conditions, two indicators, H_2 production ($PROD_{H_2}$) and specific energy consumption (SEC) [66], can also be considered. They can be calculated via Eqs. (5) and (6):

$$PROD_{H_2} = \frac{U_{H_2O} \cdot M_{H_2O} \cdot V_m \cdot 3\,600}{1\,000} \tag{5}$$

$$SEC = \frac{P_{system}}{U_{H_2O} \cdot M_{H_2O} \cdot V_m \cdot 3\,600} \tag{6}$$

where U_{H_2O} is the H_2O utilization of the system, M_{H_2O} is the molar mass of H_2O, V_m is the molar volume of the gas, and P_{system} is the total power input into the SOEC system.

3.2 Assessment of Kinetic Impacts on SOECs

To drive the water-splitting reaction, both electrical energy and thermal energy must be simultaneously supplied to the SOEC. The voltage required by the SOEC, V_{SOEC}, is the sum of the reversible potential and the additional voltage generated by all irreversible losses, which can be calculated via Eq. (7):

$$V_{SOEC} = E_{Nernst} + \eta_{act,c} + \eta_{act,a} + \eta_{ohmic} + \eta_{conc,c} + \eta_{conc,a} \tag{7}$$

where E_{Nernst} is the Nernst potential; $\eta_{act,c}$ and $\eta_{act,a}$ are the cathode and anode activation overpotentials, respectively; η_{ohimc} is the ohmic overpotential; and $\eta_{conc,c}$ and $\eta_{conc,a}$ are the cathode and anode concentration overpotentials, respectively. The Nernst equation is defined as Eq. (8):

$$E_{Nernst} = E^0 + \frac{RT}{2F}\ln\left[\frac{P^0_{H_2}\left(P^0_{O_2}\right)^{0.5}}{P^0_{H_2O}}\right] \tag{8}$$

where E^0 is the standard potential related to the SOEC temperature, R is the universal gas constant, T is the operating temperature of the SOEC, $P^0_{H_2}$ is the partial pressure of H_2, $P^0_{O_2}$ is the partial pressure of O_2, and $P^0_{H_2O}$ is the partial pressure of H_2O. E^0 can be calculated via Eq. (9) [67–69]:

$$E^0 = 1.253 - 2.541\,6 \times 10^{-4} T \tag{9}$$

where $\eta_{act,c}$, $\eta_{act,a}$, η_{ohmic}, $\eta_{conc,c}$ and $\eta_{conc,a}$ correspond to the cathode activation polarization, anode activation polarization, ohmic polarization, cathode concentration polarization, and anode concentration polarization, respectively. Figure 4 shows the sites of action of the activation, ohmic, and concentration polarizations.

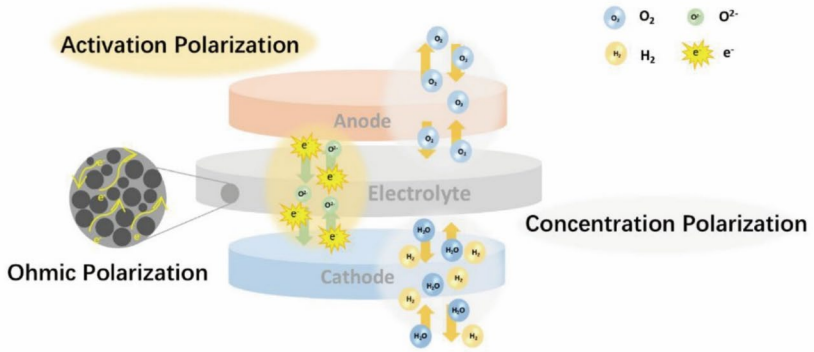

Fig. 4 Schematic of the polarization effects

Activation polarization refers to the phenomenon in which the potential of an electrode deviates from its equilibrium potential due to the delay in electrochemical reactions at the electrode, which is a fundamental form of electrode polarization. The activation loss is related to overcoming the reaction energy barrier at the electrode−electrolyte interface. The activation polarization voltage on the electrode is caused by two factors. The first is chemical transfer to activate the chemical equilibrium state of ions at the electrode−electrolyte interface. The second is electron transfer, that is, overcoming the electric field due to the transfer of charged particles at the interface. Therefore, the energy required to activate the electrolytic reaction mainly consists of chemical energy and electrical energy. The activation polarization voltage can be calculated via Butler−Volmer Eqs. (10) and (11), and the current density can be calculated via Eqs. (12), (13), and (14) [66, 70]:

$$\eta_{\mathrm{act,c}} = \frac{RT}{F}\sinh^{-1}\left(\frac{J}{2J_{0,\mathrm{c}}}\right) = \frac{RT}{F}\ln\left(\frac{J}{2J_{0,\mathrm{c}}} + \sqrt{1+\left(\frac{J}{2J_{0,\mathrm{c}}}\right)^2}\right) \tag{10}$$

$$\eta_{\mathrm{act,a}} = \frac{RT}{F}\sinh^{-1}\left(\frac{J}{2J_{0,\mathrm{a}}}\right) = \frac{RT}{F}\ln\left(\frac{J}{2J_{0,\mathrm{a}}} + \sqrt{1+\left(\frac{J}{2J_{0,\mathrm{a}}}\right)^2}\right) \tag{11}$$

$$J = \frac{2U_{\mathrm{H_2O}}M_{\mathrm{H_2O}}F}{nA} \tag{12}$$

$$J_{0,\mathrm{c}} = \kappa_{\mathrm{c}}\exp\left(\frac{-\eta_{\mathrm{act,c}}}{RT}\right) \tag{13}$$

$$J_{0,\mathrm{a}} = \kappa_{\mathrm{a}}\exp\left(\frac{-\eta_{\mathrm{act,a}}}{RT}\right) \tag{14}$$

where $\eta_{\mathrm{act,c}}$ is the cathode activation overpotential, $\eta_{\mathrm{act,a}}$ is the anode activation overpotential, n is the number of cells in the stack, A is the effective reaction area of the SOEC, κ_{c} is the pre-exponential factor for the cathode exchange current density, and κ_{a} is the pre-exponential factor for the anode exchange current density.

Ohmic polarization is caused primarily by the resistance encountered by ions migrating within the electrolyte and electrons moving across the electrodes. Since the electronic conductivity of the electrodes is much greater than the ionic conductivity of the electrolyte, the ohmic polarization is due mainly to ionic conduction within the electrolyte. Ohmic polarization is a primary cause of degradation in SOECs, and a higher ohmic resistance can affect the stability of SOECs during long-term operation [71]. In addition, the ohmic overpotential of the electrolyte dominates the total overpotential [72]. Compared with the resistance of the electrolyte, the resistance of the anode and cathode is negligible. The ohmic polarization voltage can be calculated via Eq. (15) [70, 73, 74] or directly derived from Ohm's law:

$$\eta_{\mathrm{ohm}} = 2.99\times10^{-5}\exp\left(\frac{10300}{T}\right)Jd_{\mathrm{e}} \tag{15}$$

where η_{ohm} is the ohmic overpotential and d_{e} is the electrolyte thickness.

Concentration polarization refers to the electrode polarization that occurs when the mass transfer step becomes the rate-controlling step. It is caused by the resistance to the transfer of reactants approaching the reaction site and the resistance to the transfer of products leaving the reaction site. For SOECs, the concentration polarization voltage can be represented by the difference in gas concentration between the electrode surface and the electrode–electrolyte interface and thus can be calculated via Eqs. (16) and (17) [70]:

$$\eta_{\mathrm{conc,c}} = \frac{RT}{2F}\ln\left(\frac{1+\frac{JRTd_{\mathrm{c}}}{2FD^{\mathrm{eff}}_{\mathrm{H_2O}}P^{0}_{\mathrm{H_2}}}}{1-\frac{JRTd_{\mathrm{c}}}{2FD^{\mathrm{eff}}_{\mathrm{H_2O}}P^{0}_{\mathrm{H_2O}}}}\right) \tag{16}$$

$$\eta_{\mathrm{conc,a}} = \frac{RT}{2F}\ln\left(\sqrt{1+\frac{JRTd_{\mathrm{a}}}{4FD^{\mathrm{eff}}_{\mathrm{O_2}}P^{0}_{\mathrm{O_2}}}}\right) \tag{17}$$

where d_{c} and d_{a} are the cathode and anode thicknesses, respectively, and $D^{\mathrm{eff}}_{\mathrm{H_2O}}$ is the combination of the molecular diffusion and Knudsen diffusion processes. In porous SOECs, diffusion within the electrodes is based on two main mechanisms: molecular diffusion and Knudsen diffusion [64]. When the pore diameter is much larger than the average free path of the gas molecules, molecular diffusion becomes the primary mechanism. Under these conditions, the diffusion process is controlled by molecule–molecule interactions. If the pore diameter is much smaller than the average free path of the molecules, the molecule–wall interactions dominate over the molecule–molecule interactions. Thus, Knudsen diffusion becomes the main mechanism. For most porous structures, both mechanisms are significant. The effective diffusion coefficient of steam can be represented by combining these two diffusion mechanisms and can be calculated via the Bosanquet Eq. (18) [68, 70, 73]:

$$\frac{1}{D^{\mathrm{eff}}_{\mathrm{H_2O}}} = \frac{\zeta}{\lambda}\left(\frac{1}{D_{\mathrm{H_2-H_2O}}} + \frac{1}{D_{\mathrm{H_2O},\kappa}}\right) \tag{18}$$

where $\frac{\zeta}{\lambda}$ is the ratio of the electrode tortuosity to porosity, $D_{\mathrm{H_2-H_2O}}$ is the effective molecular diffusion coefficient for the H_2–H_2O binary system, $D_{\mathrm{H_2O},\kappa}$ is the effective molecular diffusion coefficient for H_2O, and $D_{\mathrm{H_2-H_2O}}$ and $D_{\mathrm{H_2O},\kappa}$ can be obtained through kinetic theory and Chapman–Enskog theory, respectively [68].

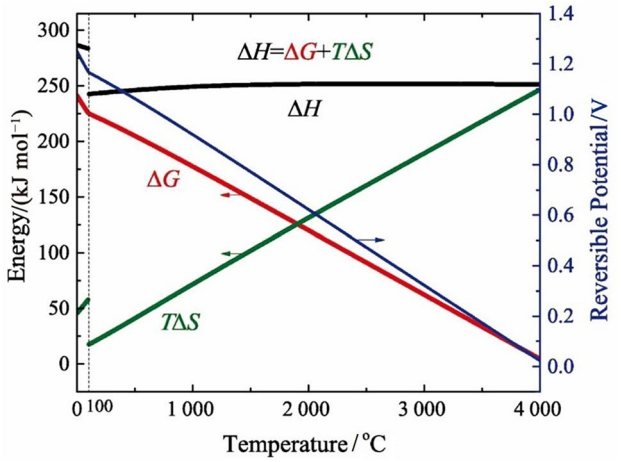

Fig. 5 Thermodynamic data of a H_2O electrolysis system. Reprinted with permission from Ref. [75]. Copyright © 2020, Elsevier

3.3 Assessment of Thermodynamic Influence in SOECs

In an ideal SOEC without any side reactions, the minimum electrical energy consumed during the electrolysis process is equal to the change in the Gibbs free energy (ΔG) [76, 77]. Therefore, the total energy consumed by the electrolysis reaction (ΔH) is the sum of the electrical energy consumed (ΔG) and the thermal energy consumed ($T\Delta S$), which can be calculated via Eq. (19):

$$\Delta H = \Delta G + T\Delta S \tag{19}$$

Figure 5 shows the thermodynamic data of a H_2O electrolysis system. The decomposition of H_2O is an endothermic reaction. As the temperature increases, the thermal energy consumed ($T\Delta S$) gradually increases, whereas the electrical energy consumed (ΔG) gradually decreases. Therefore, high-temperature SOECs require less electrical energy consumption than do low-temperature electrolysis devices. Moreover, when an SOEC operates, the irreversibility of its operation generates entropy S_{gen}, which results in additional thermal energy. S_{gen} can be calculated via Eq. (20) [70]:

$$S_{gen} = 2F(\eta_{act,c} + \eta_{act,a} + \eta_{ohmic} + \eta_{conc,c} + \eta_{conc,a}) \tag{20}$$

Therefore, the additional thermal energy generated or consumed during the operation of an SOEC system Q_{SOEC} can be calculated via Eq. (21):

$$Q_{SOEC} = (T\Delta S - S_{gen})N_{H_2O,reacted} = \frac{J}{2F}(T\Delta S - S_{gen}) \tag{21}$$

where $N_{H_2O,reacted}$ is the molar flow rate of H_2O in the reaction.

Under an operating voltage, an SOEC can be in exothermic, endothermic, or adiabatic mode. When $S_{gen} > T\Delta S$, the irreversible thermal energy of the SOEC is greater than the thermal energy required for the SOEC reaction, i.e., $Q_{SOEC} < 0$; the SOEC will be in an exothermic state and will not require an additional thermal source. When $S_{gen} < T\Delta S$, the irreversible thermal energy of the SOEC is less than the thermal energy required for the SOEC reaction, i.e., $Q_{SOEC} > 0$; the SOEC will be in an endothermic state and will require an external thermal source to supply the necessary thermal energy.

When $S_{gen} = T\Delta S$, meaning that the irreversible thermal energy of the SOEC is equal to the thermal energy required for the SOEC reaction, the SOEC will be in an adiabatic state and will neither require thermal energy from the surroundings nor radiate thermal energy to the surroundings. This condition is known as thermal neutrality, and the equilibrium voltage corresponding to the SOEC at this point is called the thermoneutral voltage [78]. The thermoneutral voltage η_{th} can be calculated via Eq. (22) [66]:

$$\eta_{th} = E_{Nernst} + \frac{T\Delta S}{2F} = \frac{\Delta H}{nF} \tag{22}$$

Notably, when an SOEC system operates at a thermoneutral voltage, the electrolysis efficiency is 100%. If the input voltage is greater than the thermoneutral voltage, the electrolysis efficiency is less than 100%. Conversely, if the input voltage is less than the thermoneutral voltage, the electrolysis efficiency is greater than 100%.

3.4 SOEC Efficiency Assessment from a Solar Energy Perspective

During the process of driving an SOEC with solar energy as the power source, solar energy is converted into electrical and thermal energy. Electrical energy is generated by photovoltaic panels, whereas thermal energy is derived from the direct concentration of solar irradiance. In terms of utilization methods, SOEC systems that exploit both thermal and nonthermal effects can employ three distinct methods: direct irradiation, spectral splitting, and synergistic response.

The utilization of direct irradiation involves two beams of sunlight irradiating a photovoltaic panel and a heat collector to generate electrical energy and thermal energy (Fig. 6a). However, photovoltaic panels can convert light only in a specific wavelength range (ultraviolet and partially visible light) into electrical energy, with light beyond this range dissipating directly as heat. A heat collector can convert light into thermal energy. According to the second law of thermodynamics, heat generation increases irreversible losses and reduces the quality

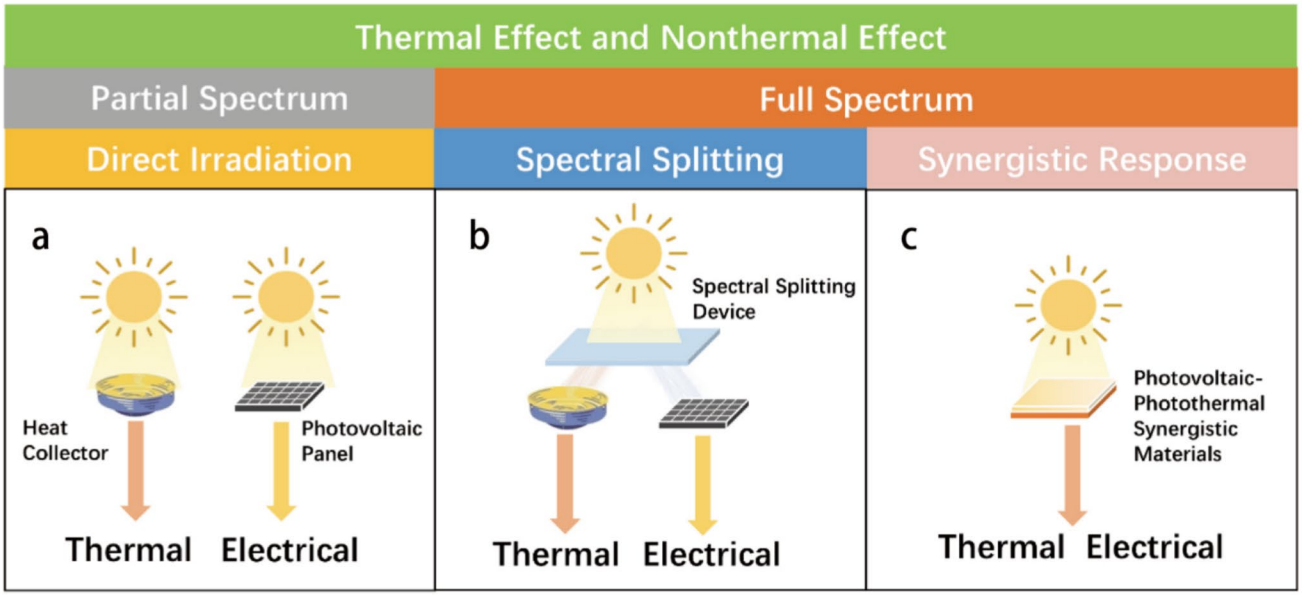

Fig. 6 Types of SOEC solar energy harnessing techniques

of energy. Considering the potential of high-energy photons, the use of the full spectrum for heating seems to be wasteful [39]. From a system design perspective, it is easy to implement the direct irradiation of two devices using two beams of sunlight, but this method utilizes only a partial spectrum, resulting in low solar-energy utilization efficiency. To utilize the full spectrum, the balance between the photoelectric and photothermal conversion performances should be determined. We can use a spectral splitting device to divide sunlight [79]. In spectral splitting, a beam of light is separated into light of different wavelengths via a spectral splitting device, where shorter-wavelength light (ultraviolet and partially visible light) is directed to the photovoltaic panels for electricity generation and longer-wavelength light (infrared and partially visible light) is directed toward a heat collector for heat generation (Fig. 6b). This method can effectively enhance the system's solar-to-fuel efficiency, and further improvements in the structure of the spectral splitting device and the optical path of the system are needed. The synergistic response method requires the development of photovoltaic and photothermal synergistic materials to absorb solar light of different wavelengths (Fig. 6c). The photovoltaic response layer of the material absorbs a portion of the light, exploiting the photoelectric effect to provide electrical energy, whereas the remaining light is transmitted through the photovoltaic response layer and is absorbed by the photothermal response layer, where it is converted into thermal energy. Unlike spectral splitting, the synergistic response method does not require a dedicated spectral splitting device but instead achieves full-spectrum conversion through the inherent properties of materials. It is necessary to design suitable multifunctional-layer materials and synergize the thermal and nonthermal effects within a single material.

Assuming that all the energy required for an SOEC is supplied by solar energy, we can construct the following formulas to analyze the efficiency of the existing solar energy conversion methods.

In the method depicted in Fig. 6a, the STF efficiency η_{solar1} can be calculated via Eq. (23):

$$\eta_{solar1} = \frac{LHV \cdot N_{out}}{\frac{Q_t}{\xi_t} + \frac{Q_e}{\xi_e}} \tag{23}$$

where Q_t is the thermal energy required by the SOEC, Q_e is the electrical energy required by the SOEC, ξ_t is the solar thermal concentration efficiency factor, and ξ_e is the photovoltaic conversion efficiency factor.

In the method depicted in Fig. 6b, the STF efficiency η_{solar2} can be calculated via Eq. (24):

$$\eta_{solar2} = \frac{LHV \cdot N_{out}}{\frac{\frac{Q_t}{\varphi_t} + \frac{Q_e}{\varphi_e}}{\alpha}} \tag{24}$$

where φ_t is the solar thermal concentration efficiency factor after spectral splitting, φ_e is the photovoltaic conversion efficiency factor after spectral splitting, and α is the loss coefficient of the spectral splitting device.

Comparing η_{solar1} with η_{solar2}, it is evident that through the utilization of spectrally split solar energy, ξ_t and ξ_e are certainly greater than the factors φ_t and φ_e. This is attributed to the fact that after spectral splitting, the

short-wavelength part of the spectrum is largely absorbed by the solar cells to induce the photovoltaic effect, while the thermal-concentration effect for long-wavelength light is also more pronounced. Therefore, the prospects for coupling spectral-splitting devices with SOECs for chemical reactions are exceedingly promising.

In the method depicted in Fig. 6c, the STF efficiency η_{solar3} can be calculated via Eq. (25):

$$\begin{cases} \eta_{solar3} = \dfrac{LHV \cdot N_{out}}{\frac{Q_e}{\mu_e}} = \dfrac{LHV \cdot N_{out}}{\frac{\beta Q_t}{(1-\mu_e-\gamma_e)\mu_t}} & (\beta \geqslant 1) \\ \beta = \dfrac{(1-\mu_e-\gamma_e)\mu_t Q_e}{\mu_e Q_t} \end{cases} \quad (25)$$

where μ_e is the photovoltaic conversion efficiency factor of photovoltaic synergistic materials, μ_t is the thermal conversion efficiency factor of photothermal synergistic materials, γ_e is the transmission loss coefficient of the photovoltaic response layer and β is the synergistic response coefficient, which is related to the synergistic effect of the composite material.

When $\beta \geqslant 1$, the solar energy transmitted through the photoelectric material layer to the photothermal response layer is sufficient to provide all the thermal energy required by the SOEC. Conversely, when $0 \leqslant \beta < 1$, the solar energy reaching the photothermal response layer after passing through the photoelectric material layer falls short of the thermal demand. Under these conditions, additional solar energy input is necessary, which may result in surplus electrical energy being wasted in the photoelectric response layer.

A comparison of η_{solar2} with η_{solar3} clearly reveals that the approach depicted in Fig. 6c, which does not involve the use of a spectral splitting device, effectively mitigates the spectral splitting loss associated with α, thereby increasing the actual solar energy input into the system [80]. In the synergistic response method, the photovoltaic and photothermal response capabilities of the material are directly related to μ_e, μ_t, and γ_e, significantly affecting the overall STF efficiency. Therefore, the selection of responsive materials becomes particularly crucial. Maximizing the utilization of both the thermal and non-thermal effects of solar energy to achieve direct use of the full solar spectrum is imperative. Currently, research on synergistic response materials for solid oxide electrolysis cells (SOECs) in solar energy applications is relatively scarce, necessitating greater research efforts and attention from the scientific community in this area.

Furthermore, in traditional SOEC reaction systems, the thermoneutral voltage is widely recognized as the most suitable voltage for the SOEC, at which the energy input is minimized. However, in solar-driven SOEC systems, owing to the inevitable thermal energy generation from solar irradiation, adjusting the input voltage to a level slightly lower than the thermoneutral voltage, thereby ensuring that the SOEC operates in an endothermic state, may be more compatible with solar-driven systems.

4 Current Status of SOEC Systems

4.1 Modeling of Existing SOEC Systems

In recent years, substantial progress has been made in the field of SOECs. Despite these advancements, there is an ongoing need for optimized designs of electrode materials and structures. A deep understanding of the electrochemical/chemical processes and the transport of mass, heat, and charge within an SOEC is crucial for improving the performance and system efficiency [81]. Numerical models of SOEC systems can be utilized to investigate and predict material properties, thereby guiding the optimization of actual materials and structural designs. Hence, it is imperative to establish a comprehensive understanding of the modeling of existing SOEC systems.

Currently, SOEC system models can be built from three aspects: one-dimensional (1D), two-dimensional (2D), and three-dimensional (3D). A one-dimensional model does not require complex data such as flow and temperature fields. Instead, processes related to chemical equilibrium, electrochemistry, and energy conservation, involving multicomponent diffusion and electrochemical processes, are integrated. In such a model, empirical formulas and related laws are used to explain various parameters, thereby predicting the performance of an SOEC. This type of model is particularly suitable for predicting the material composition and electrochemical performance because it requires minimal computational resources and does not need to consider the two- or three-dimensional spatial distribution within the SOEC. Only the flow of energy and matter from thermodynamic and kinetic perspectives needs to be analyzed. Lu et al. proposed a temperature control strategy tailored for different operating current densities. By constructing a one-dimensional model of an SOEC, they elucidated the relationship between the inlet gas flow rate and the cell temperature, thereby enabling rapid stabilization of the operating temperature under actual fluctuating current conditions [67]. Tanaka et al. developed a quasi-1D simulation model to assess the gas conversion impedance within an SOEC, which facilitated a better evaluation of the overvoltage. The simulated voltages obtained were compared with the measured voltages, demonstrating a precision level of $\pm 0.3\%$ [82]. Menon et al. developed a one-dimensional electrochemical model to study the co-electrolysis of H_2O and CO_2 and explored the impacts of the operating temperature, porosity, cathode thickness, inlet gas velocity, and type of electrolysis on the reaction [83]. Li et al. simulated the co-electrolysis of H_2O and CO_2 considering the

coupling and competitive effects of heterogeneous chemical reactions and electrochemical reactions and investigated the influence of the cathode porosity, microstructure, gas composition, and temperature on the reaction [84]. Samavati et al. proposed a thermodynamic model for a pressurized SOEC system and analyzed and quantified the effects of the operating pressure on the SOEC system performance from five perspectives: pressure, temperature, reactant utilization rates, relative irreversibility, and economics [12]. For the current one-dimensional models, a univariate approach to analyzing the SOEC reactions is often adopted, either by assessing the overall system from the perspective of a single influencing factor or by studying the effect of one specific variable on another variable within the SOEC context. Consequently, there is a need for future studies to explore the synergistic effects and impacts of a multitude of conditions on the efficiency of SOEC systems, moving toward a more holistic understanding of their performance dynamics.

A two-dimensional model accounts for the material flow field, and a heat-transfer model is constructed to analyze the energy flow and boundary conditions of the system to explain the macroscopic operation of the system from the perspective of heat transfer. Ni et al. developed a two-dimensional thermal-fluid model consisting of a 1D model and a computational fluid dynamics model to study CO_2 electrolysis and investigated the effects of the inlet gas velocity, electrode permeability, and inlet gas composition on SOEC performance. They reported that below the thermoneutral-voltage threshold of 1.463 V at 1 173 K, the average electrolyte temperature first decreases with increasing operating potential, reaches a minimum at approximately 1.1 V, and subsequently increases as the potential continues to increase [72]. Nerat et al. modeled a two-dimensional axisymmetric structure of an SOEC to study the effects of a partly delaminated anode on the electrochemical performance [85]. Currently, only a few researchers use two-dimensional models for SOECs. Although these models work well for small problems, they are less effective for larger or more complex systems because of the limitations of the boundary conditions.

4.2 Performance of Typical SOEC Systems

To understand the current state and development of SOEC models, it is necessary to conduct an initial comprehensive examination and evaluation of the current performance of SOECs. This involves not only understanding the existing technical parameters, such as the electrochemical performance, energy conversion efficiency, and durability over long-term operation, but also analyzing the performance of SOECs under typical operating conditions.

For H-SOECs, researchers have focused on exploring materials that can reduce the temperature required for the reaction, especially those seeking electrolytes with a higher ionic conductivity at lower temperatures. This can increase the current density of SOECs at reduced temperatures, allowing SOECs to be coupled with waste thermal energy from industrial production for utilization, thereby improving the overall efficiency of the system. For O-SOECs, researchers are committed to enhancing the system performance through various strategies, such as electrochemical-activity enhancement and electrode-material optimization.

Notably, many R-SOCs, which can perform both electrolysis and fuel cell operations, have already demonstrated impressive performance. These devices can operate at lower temperatures than traditional electrolysis technologies while achieving higher current densities. This means that, while providing the same electrolysis capability, they can be more energy-efficient and have the potential to play a role in a broader range of applications.

Table 1 and Fig. 7 present the performance of several representative SOEC H_2O electrolysis systems examined in recent years. To date, the peak current density of SOECs under 1.3 V has surpassed 5 A cm^{-2}. However, the current density for H_2O electrolysis in most SOECs is primarily concentrated in the range of 0–2.5 A cm^{-2}. Among these exemplary SOECs, Hu et al. reported an air electrode with a nominal composition of $PrBa_{0.8}Ca_{0.2}Fe_{1.8}Ce_{0.2}O_{6-\delta}$ in a reversible protonic ceramic electrochemical cell (R-PCEC). This cell demonstrated exceptionally high performance with a current density of 5.00 A cm^{-2} at 1.3 V and 700 °C in the electrolysis mode, as shown in Fig. 8a [88]. Nonetheless, stability tests conducted at 500 mA cm^{-2} and 650 °C revealed that the electrode's stability was limited to only 95 h, indicating that a significant gap remains before practical commercial application. Luo et al. reported a single cell based on $BaNb_{0.05}Ce_{0.7}Yb_{0.25}O_{3-\delta}$ that achieved high current densities of 3.22 A cm^{-2} at 650 °C and 2.24 A cm^{-2} at 600 °C under 1.3 V, as shown in Fig. 8b [89]. Notably, this cell exhibited no obvious degradation in performance during a long-term stability test in the electrolysis mode (0.5 A cm^{-2}, 500 °C) for 800 h, indicating prominent advancements in the field of middle-temperature SOECs in recent years.

Achieving enhanced electrochemical performance at lower temperatures continues to be a significant challenge. Currently, many researchers are actively exploring SOEC H_2O electrolysis at intermediate temperatures. However, few studies exist on the performance of SOECs at temperatures below 450 °C. Liu et al. developed a PCEC with an in-situ-formed composite cathode, which showed remarkable current densities in steam electrolysis mode (1.28 A cm^{-2} at 1.4 V and 450 °C). The cell sustained stable operation for a notable duration of more than 250 h at 400 °C with a current density of 600 mA cm^{-2}, as shown in Fig. 8d [60]. Moreover, Bian et al. conducted tests on a PCEC that underwent acid etching treatment within the temperature interval of 350–600 °C. They reported that this

Table 1 Summary of SOECs for H_2O electrolysis

Electrolyte	Steam electrode	Hydrogen electrode	Temperature/°C	Current density @1.3 V/(A cm^{-2})	Stability	References
$BaZr_{0.7}Ce_{0.2}Y_{0.1}O_{2.95}$ (BCZY72)	$BaGd_{0.8}La_{0.2}Co_2O_{6-\delta}$-BCZY72	Ni-BCZY72	600	0.097	No degradation for 700 h, 62.5 mA cm^{-2} at 600 °C	[32]
$BaCe_{0.4}Zr_{0.4}Y_{0.1}$ $Yb_{0.1}O_{3-\delta}$ (BCZYYb4411)	3D $PrNi_{0.5}Co_{0.5}O_{3-\delta}$	Ni-BCZYYb4411	600 500 400	1.18 0.56 0.23	10% increase for 120 h, 1.4 V at 600 °C	[47]
$BaCe_{0.4}Zr_{0.4}Y_{0.1}$ $Yb_{0.1}O_{3-\delta}$ (BCZYYb4411)	$PrBa_{0.5}Sr_{0.5}Co_{1.5}Fe_{0.5}O_{5+\delta}$	Ni-BCZYYb4411	600 500	1.42 0.40	No degradation for 500 h, 1.3 V at 550 °C	[93]
$BaZr_{0.1}Ce_{0.7}Y_{0.2-x}Yb_xO_{3-\delta}$ (BZCYYb1711)	$PrBa_{0.5}Sr_{0.5}Co_{2-x}Fe_xO_{5+\delta}$	Ni-BZCYYb1711	600 550 500	0.85 0.42 0.21	Constant activation for 70 h, 1.6 V at 500 °C	[94]
$BaCe_{0.7}Zr_{0.1}Y_{0.1}Yb_{0.1}O_{3-\delta}$ (BCZYYb7111)	$BaCo_{0.4}Fe_{0.4}Zr_{0.1}Y_{0.1}O_{3-\delta}$	Ni-BCZYYb7111	600 550 500	0.90 0.70 0.50	0.03 mV per hour degradation for 1 200 h, 1385 mA cm^{-2} at 550 °C	[20]
$BaHf_xCe_{0.8-x}Y_{0.1}Yb_{0.1}O_{3-\delta}$ (BHCYYb3511)	$PrBa_{0.5}Sr_{0.5}Co_{1.5}Fe_{0.5}O_{5+\delta}$	Ni-BHCYYb3511	600	1.45	No degradation for 1 000 h, 1 000 mA cm^{-2} at 600 °C	[90]
$BaZr_{0.2}Ce_{0.6}Y_{0.2}O_{3-\delta}$ (BZCY)	$Pr_2NiO_{4+\delta}$-BCZY	Ni-BCZY	700 600	0.977 0.600	No data	[95]
$BaZr_{0.1}Ce_{0.7}Y_{0.1}Yb_{0.1}O_{3-\delta}$ (BZCYYb1711)	$Ba_{0.9}Co_{0.7}Fe_{0.2}Nb_{0.1}O_{3-\delta}$	Ni-BZCYYb1711	650 600 550 500	2.8 1.6 0.7 0.3	No degradation for 100 h, 500 mA cm^{-2} at 600 °C	[33]
$BaCe_{0.4}Zr_{0.4}Y_{0.1}$ $Yb_{0.1}O_{3-\delta}$ (BCZYYb4411)	$(PrBa_{0.8}Ca_{0.2})_{0.95}Co_2O_{6-\delta}$	Ni-BCZYYb4411	600 550 500	0.72 0.39 0.16	No degradation for 160 h, 1.3 V at 500 °C	[96]
$BaZr_{0.6}Ce_{0.2}Y_{0.1}Yb_{0.1}O_{3-\delta}$ (BZCYYb6211)	$La_{0.8}Sr_{0.2}Co_{0.7}Ni_{0.3}O_{3-\delta}$-$La_{0.5}Sr_{0.5}CoO_{3-\delta}$	Ni-BZCYYb6211	600	1.22	1% increase for 100 h, 1 000 mA cm^{-2} at 500 °C	[97]
$BaZr_{0.1}Ce_{0.7}Y_{0.1}Yb_{0.1}O_{3-\delta}$ (BZCYYb1711)	$PrBa_{0.8}Ca_{0.2}Co_2O_{5+\delta}$-$BaCoO_{3-\delta}$	Ni-BZCYYb1711	650 600 550	2.52 1.51 0.69	4.0% per 1 000 h degradation for 1 500 h, 1 000 mA cm^{-2} at 600 °C	[92]
$BaZr_{0.1}Ce_{0.7}Y_{0.1}Yb_{0.1}O_{3-\delta}$ (BZCYYb1711)	$(La_{0.6}Sr_{0.4})_{0.95}Co_{0.2}Fe_{0.8}O_{3-\delta}$-$Pr_{1-x}Ba_xCoO_{3-\delta}$	Ni-BZCYYb1711	650 600 550	3.13 1.82 0.85	No degradation for 300 h, 1 000 mA cm^{-2} at 600 °C	[98]
$BaNb(Ta)_{0.05}Ce_{0.7}Yb_{0.25}O_{3-\delta}$ (BNCYb)	$PrBa_{0.8}Ca_{0.2}Co_2O_{5+\delta}$ (PBCC)	Ni-BNCYb	650 600 550 500	3.22 2.24 1.21 0.69	No obvious degradation for 800 h, 500 mA cm^{-2} at 500 °C	[89]
$BaZr_{0.1}Ce_{0.7}Y_{0.1}Yb_{0.1}O_{3-\delta}$ (BZCYYb1711)	$PrBa_{0.8}Ca_{0.2}Fe_{1.8}Ce_{0.2}O_{6-\delta}$ (PBCFC)	NiO-BZCYYb1711	700 650 600	5.00 3.45 1.73	No degradation for 95 h, 500 mA cm^{-2} at 650 °C	[88]
$BaZr_{0.1}Ce_{0.7}Y_{0.1}Yb_{0.1}O_{3-\delta}$ (BZCYYb1711)	$PrBa_{0.8}Ca_{0.2}Fe_2O_{6-\delta}$ (PBCF)	NiO-BZCYYb1711	700 650 600	3.12 1.92 0.94	2.36 mV per hour degradation for 50 h, 500 mA cm^{-2} at 650 °C	[88]
$BaZr_{0.1}Ce_{0.7}Y_{0.1}Yb_{0.1}O_{3-\delta}$ (BZCYYb1711)	$Ba_{0.8}Gd_{0.8}Pr_{0.4}Co_2O_{5+\delta}$-$Gd_xCo_yO_{3-\delta}$	Ni-BZCYYb1711	700 650 600	3.485 2.336 1.323	No obvious degradation for 200 h, 500 mA cm^{-2} at 650 °C	[99]
$(Li_{0.67}Na_{0.33})_2CO_3$-$Sm_{0.2}Ce_{0.8}O_2$	$Pr_{0.4}Ba_{0.2}Ca_{0.2}La_{0.2}Co_{0.2}Fe_{0.8}O_3$ (PBCLCF)	PBCLCF	700 650 600 550	0.647 3 0.484 1 0.312 6 0.192 4	No data	[100]
$La_{0.8}Sr_{0.2}Ga_{0.8}Mg_{0.2}O_{3-\delta}$	$La_{0.6}Sr_{0.4}Co_{0.2}Fe_{0.8}O_{3-\delta}$-$Gd_{0.1}Ce_{0.9}O_{2-\delta}$	$Sr_2FeCo_{0.2}Ni_{0.2}Mo_{0.6}O_{6-\delta}$- $Gd_{0.1}Ce_{0.9}O_{2-\delta}$	800 750 700	0.94 0.58 0.37	No degradation for 150 h, 200 mA cm^{-2} at 750 °C	[101]
$BaCe0_{.68}Zr_{0.1}Y_{0.1}Yb_{0.1}Cu_{0.02}O_{3-\delta}$(BCZYYC2)	$La_{1.2}Sr_{0.8}NiO_{4-\delta}$-BCZYYC2	Ni-BCZYYC2-carbon microspheres	700 650 600	3.02 1.87 1.04	No degradation for 100 h, 1.3 V at 700 °C	[102]
YSZ	$Pr_{1.39}Ba_{0.14}Sr_{0.53}Co_{1.48}Fe_{0.76}O_{6-\delta}$-$Ba_{0.66}Sr_{0.34}CoO_{3-\delta}$	NiO-YSZ	750	4.4	3 mV per hour degradation for 60 h, 800 mA cm^{-2} at 650 °C	[103]
YSZ	$Sm_{0.5}Sr_{0.5}CoO_{3-\delta}$-$Ce_{0.8}Sm_{0.2}O_{1.9}$	Ni-YSZ	800 750	4.08 3.13	No degradation for 40 h, 1 000 mA cm^{-2} at 750 °C	[22]

Table 1 (continued)

Electrolyte	Steam electrode	Hydrogen electrode	Temperature/°C	Current density @1.3 V/(A cm^{-2})	Stability	References
YSZ	$Sr(Ti_{0.3}Fe_{0.7-x}Co_x)O_{3-\delta}$	Ni-YSZ	800 700 600	3.03 1.48 0.51	No obvious degradation for 350 h, for 1 000, 1 200, 1 500 mA cm^{-2} at 700 °C	[104]
YSZ	$Pr_{0.8-x}Bi_xSr_{0.2}MnO_{3-\delta}$	Ni-YSZ	750 700 650 600	2.71 1.86 0.88 0.60	No obvious degradation for 450 h, 250 mA cm^{-2} at 700 °C	[105]
ScSZ	$PrBa_{0.5}Sr_{0.5}Co_{1.5}Fe_{0.5}O_{5+\delta}$-$Gd_{0.1}Ce_{0.9}O_2$	Ni-YSZ	750 700 650 600	2.10 1.45 0.94 0.51	No degradation for 1 000 h, 200 mA cm^{-2} at 700 °C	[106]
YSZ	$La_{0.8}Sr_{0.2}MnO_{3-\delta}$-Y co-doped Bi_2O_3	Ni-YSZ	700 650 600	1.32 0.91 0.46	No degradation for 100 h, 1 000 mA cm^{-2} at 700 °C	[91]
YSZ	$La_{0.6}Sr_{0.4}Co_{0.2}Fe_{0.8}O_{3-\delta}$-$Sm_{0.075}Nd_{0.075}Ce_{0.85}O_{2-\delta}$	Ni-YSZ	750 700	1.37 0.97	No degradation for 300 h, 200 mA cm^{-2} at 700 °C	[107]
YSZ	$PrBa_{0.5}Sr_{0.5}Co_{1.5}Fe_{0.5}O_{5+\delta}$-$Gd_{0.1}Ce_{0.9}O_2$	Ni-YSZ	800 700	2.75 1.27	No degradation for 300 h, 300 mA cm^{-2} at 700 °C	[108]
YSZ	$PrBaFe_{1.9}Zr_{0.1}O_{5+\delta}$-$Gd_{0.1}Ce_{0.9}O_2$	Ni-YSZ	700	2.21	No degradation for 100 h, 180 mA cm^{-2} at 700 °C	[109]

Note: Data are extracted from different resources, thus with different significant digits

method can effectively rejuvenate the electrolyte surface after high-temperature annealing, which in turn increases the electrochemical performance. This PCEC exhibited stable electrolysis operations with current densities surpassing 3.9 A cm^{-2} at 1.4 V and 600 °C, as shown in Fig. 8d [110].

From Fig. 7, we can obtain Eq. (26) based on Ohm's law:

$$I = \frac{U}{\rho(M, T, C)} \tag{26}$$

where U is the external voltage, ρ is the resistivity of the SOEC, and I is the current density.

U can be supplied through photovoltaic panels or an external power source, and ρ is related to three factors: material, temperature, and the coupling method. The field of materials science has already undergone a plethora of studies focused on material modification and doping to increase SOEC performance [89–91, 111, 112]. By applying the functional relationship between electrical conductivity and temperature (thickness of 100 μm), we can map the current density trend at 1.3 V, as shown in Fig. 7. This trend closely mirrors the typical performance trend of SOECs reported in the literature, particularly for the widely adopted proton-conducting electrolyte $BaZr_{0.1}Ce_{0.7}Y_{0.1}Yb_{0.1}O_{3-\delta}$ [90]. Additionally, $BaZr_{0.4}Ce_{0.4}Y_{0.1}Yb_{0.1}O_{3-\delta}$ has shown remarkable conductivity at 500 °C [112], whereas materials such as yttria-stabilized zirconia (YSZ) [91], $BaZr_{0.5}Ce_{0.3}Y_{0.1}Yb_{0.1}O_{3-\delta}$ [89], and $BaZr_{0.55}Ce_{0.3}Y_{0.15}O_{3-\delta}$ [111] lag behind in conductivity, hinting at their potential limitations for SOEC applications at lower temperatures.

As detailed in Sect. 3.2, ohmic polarization is identified as the primary culprit behind SOEC degradation and is predominantly influenced by the electrolyte conductivity. This suggests that the performance of current SOECs may have reached a plateau, underscoring the urgent need for innovation in electrolyte materials. Temperature plays a dual role: it affects both the thermodynamics of the SOEC reaction, as discussed in Sect. 3.3, and the current density by influencing the electrolyte conductivity. Additionally, the methods of coupling solar energy to SOECs have the potential to markedly influence energy efficiency, as depicted in Fig. 6. The field of solar-driven SOECs remains largely unexplored. Consequently, this review focuses on methods for solar energy integration with SOECs in Sect. 5, with the goal of revealing novel pathways to optimize electrolysis efficiency.

4.3 Stability Analysis of Typical SOEC Systems

Degradation issues hinder the long-term operation of SOECs, and their long-term stable operation can significantly reduce costs. The degradation of an SOEC is related mainly to the following factors [37].

Local overpotentials: Local overpotentials at active sites within the cell, which are caused by excessively high or low oxygen activity, are directly related to degradation, such as the formation of O_2 bubbles in the electrolyte, delamination at the electrolyte/air-electrode interface, Si poisoning of the fuel electrode, and Zr nanoparticle poisoning of Ni at the fuel electrode [113, 114].

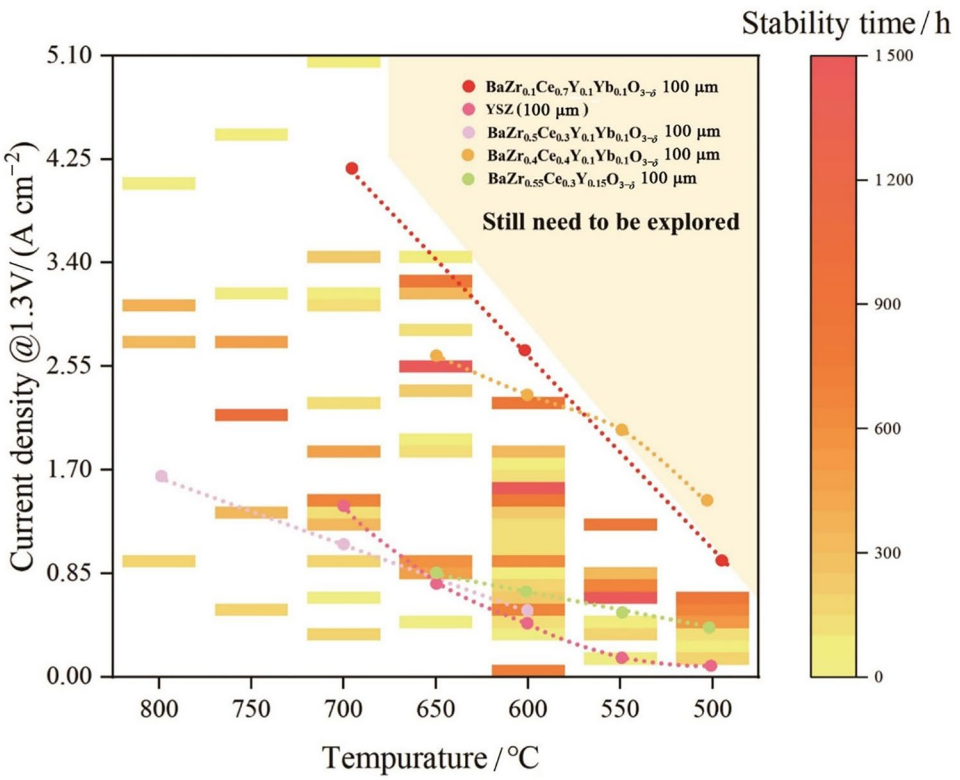

Fig. 7 Performance of representative SOECs for H_2O electrolysis. [20, 21, 32, 33, 47, 88–109]

Gas composition: Variations in the local gas composition, especially in the electrode thickness direction, can affect the progress of electrochemical reactions, thereby impacting cell degradation.

Temperature and thermal gradients: The operating temperature and thermal gradient within a cell significantly affect the performance and degradation of an SOEC. A non-uniform temperature distribution can lead to thermal stress and thermal fatigue in materials, resulting in degradation.

Current density: An increase in the current density may lead to accelerated electrode reactions, increased local overpotential, and thus accelerated degradation.

Operating cell voltage: The operating voltage of the cell, whether below or above the thermoneutral voltage, affects the thermal behavior of the cell, which in turn affects degradation. A low voltage may lead to endothermic behavior, whereas a high voltage may lead to exothermic behavior.

Material properties of electrodes and electrolyte: The choice of materials for electrodes and the electrolyte, manufacturing processes, particle size, porosity, and tortuosity can affect degradation.

Gas flow rates: The magnitude of the gas flow rate affects the transport and distribution of gases within the cell, which in turn affects the efficiency of electrochemical reactions and degradation.

Cell geometry: The geometry of the cell, including the thicknesses of the electrodes and electrolyte, also affects the degradation process.

Cell polarization: The cell polarization, geometry, operating parameters, and radiative heat loss affect the performance and degradation of a cell.

Liu et al. developed a PCEC with an in-situ-formed composite cathode. In electrolysis mode, it can operate stably for more than 250 h at 400 °C with a working current density of 600 mA cm^{-2}, as shown in Fig. 9a [60]. Shao et al. reported a full-size Ni-YSZ cell unit that operated for 336 h at a current density of 2 A cm^{-2}, demonstrating the feasibility of operating an SOEC at high current densities, as shown in Fig. 9b [115]. Duan et al. proposed a reversible PCEC based on a yttrium- and ytterbium-codoped barium-zirconate electrolyte and a tri-electroconductive oxide air/steam reversible electrode. In the electrolysis mode, the PCEC maintained a current density of 1 385 mA cm^{-2}, and the device was subjected to stability tests for 1 200 h at 550 °C. Researchers reported that the reduction in the FE was negligible and that the low voltage drop rate was less than 30 mV per 1 000 h, as shown in Fig. 9c [20]. Zhou et al. reported an air electrode composed of $PrBa_{0.8}Ca_{0.2}Co_2O_{5+\delta}$ and in-situ-precipitated $BaCoO_{3-\delta}$ nanoparticles, which had the lowest polarization resistance (approximately 0.24 Ω cm^2) at 600 °C and high stability in humid air with 3%–50% H_2O. This PCEC performed well at 600 °C, achieving a current density of 1.51 A cm^{-2} at 1.3 V in the electrolysis mode. More importantly, the PCEC demonstrated exceptionally high durability, with over 1 833 h of continuous operation in electrolysis mode, as shown in Fig. 9d [92].

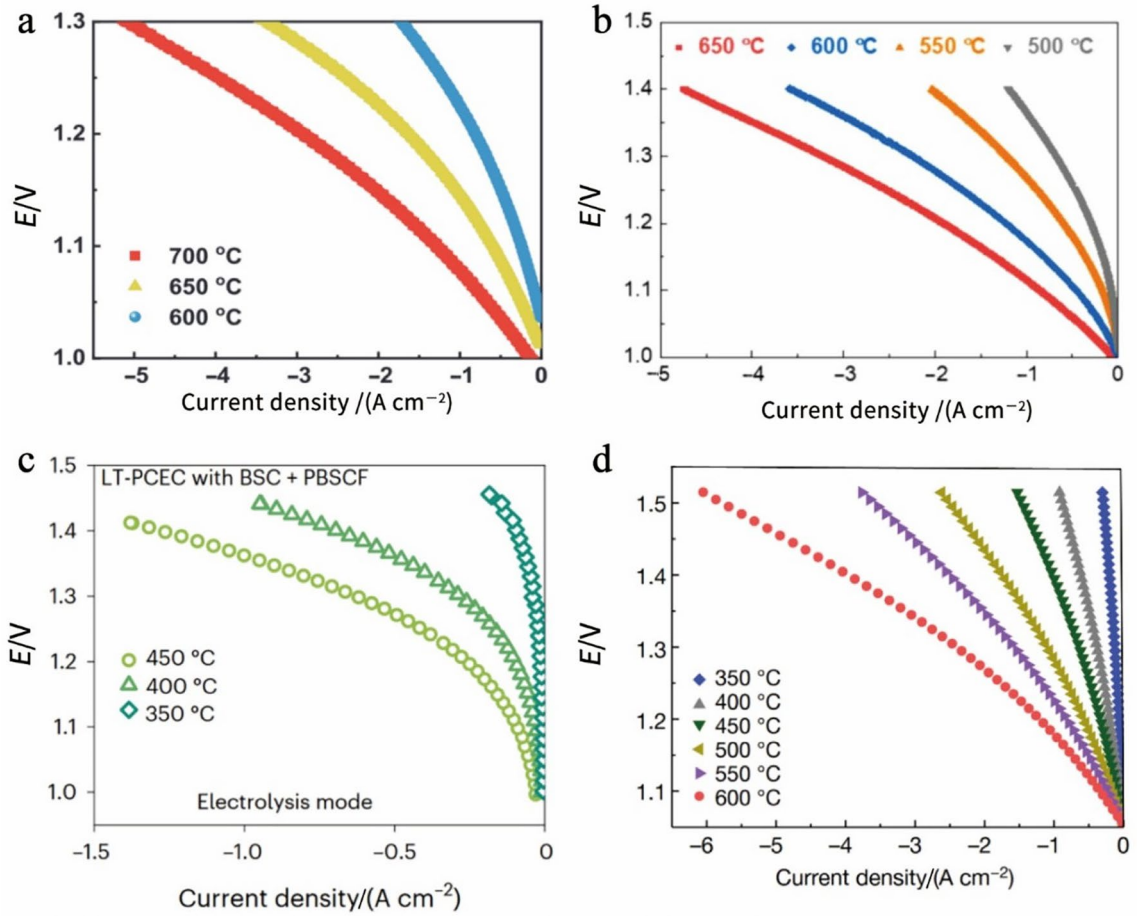

Fig. 8 **a** Typical $I-V$ curves of $PrBa_{0.8}Ca_{0.2}Fe_{1.8}Ce_{0.2}O_{6-\delta}$|$BaZr_{0.1}Ce_{0.7}Y_{0.2-x}Yb_xO_{3-\delta}$|NiO-$BaZr_{0.1}Ce_{0.7}Y_{0.2-x}Yb_xO_{3-\delta}$ for hydrogen production at 600–700 °C. Reprinted with permission from Ref. [88]. Copyright © 2023, John Wiley and Sons. **b** Typical $I-V$ curves of $PrBa_{0.8}Ca_{0.2}Co_2O_{5+\delta}$|$BaNb(Ta)_{0.05}Ce_{0.7}Yb_{0.25}O_{3-\delta}$|Ni-$BaNb(Ta)_{0.05}Ce_{0.7}Yb_{0.25}O_{3-\delta}$ for hydrogen production at 500–650 °C. Reprinted with permission from Ref. [89]. Copyright © 2022, American Chemical Society. **c** Typical $I-V$ curves of $Ba_{0.62}Sr_{0.38}CoO_{3-\delta}$-$Pr_{1.44}Ba_{0.11}Sr_{0.45}Co_{1.32}Fe_{0.68}O_{6-\delta}$|$BaCe_{0.7}Zr_{0.1}Y_{0.1}Yb_{0.1}O_{3-\delta}$|NiO-$BaCe_{0.7}Zr_{0.1}Y_{0.1}Yb_{0.1}O_{3-\delta}$ for hydrogen production at 350–450 °C. Reprinted with permission from Ref. [60]. Copyright © 2023, Springer Nature. **d** Typical $I-V$ curves of $PrNi_{0.7}Co_{0.3}O_{3-\delta}$|$BaZr_{0.4}Ce_{0.4}Y_{0.1}Yb_{0.1}O_{3-\delta}$|NiO-$BaZr_{0.4}Ce_{0.4}Y_{0.1}Yb_{0.1}O_{3-\delta}$ for hydrogen production at 350–600 °C. Reprinted with permission from Ref. [110]. Copyright © 2022, Springer Nature

Figure 7 clearly shows that under conditions of high temperature and high current density, the stability of existing SOECs requires enhancement. In the 700–800 °C temperature bracket, the majority of SOECs exhibit less than 300 h of stability, with a mere handful exceeding the 1 000 h threshold. As the reaction temperature decreases, the stability of the SOECs appears to improve, but this improvement is accompanied by a significant decrease in the current density. A qualified SOEC material should maintain its integrity, i.e., show no degradation, for a minimum of 100 h. To date, some SOECs have demonstrated remarkable stability, enduring over 1 000 h of continuous operation without any detectable performance decline. The cornerstone of enhancing the stability lies in refining the electrode materials and optimizing the electrode configuration, which are critical for the enduring performance and resilience of SOECs in practical applications.

5 Solar Energy Integration with SOEC Systems

After insights into the current state and performance of SOECs are gained, further exploration of how to integrate SOECs with solar energy is essential. Understanding the mechanisms of SOECs coupled with solar energy systems will elucidate their potential development directions and opportunities for future improvements. This exploration is crucial for harnessing the full potential of the SOEC technology and pushing the boundaries of what is possible in the realm of energy conversion and efficiency. Table 2 presents representative SOEC-coupled solar energy systems developed in recent years. The existing methods for coupling SOECs with solar energy are primarily divided into

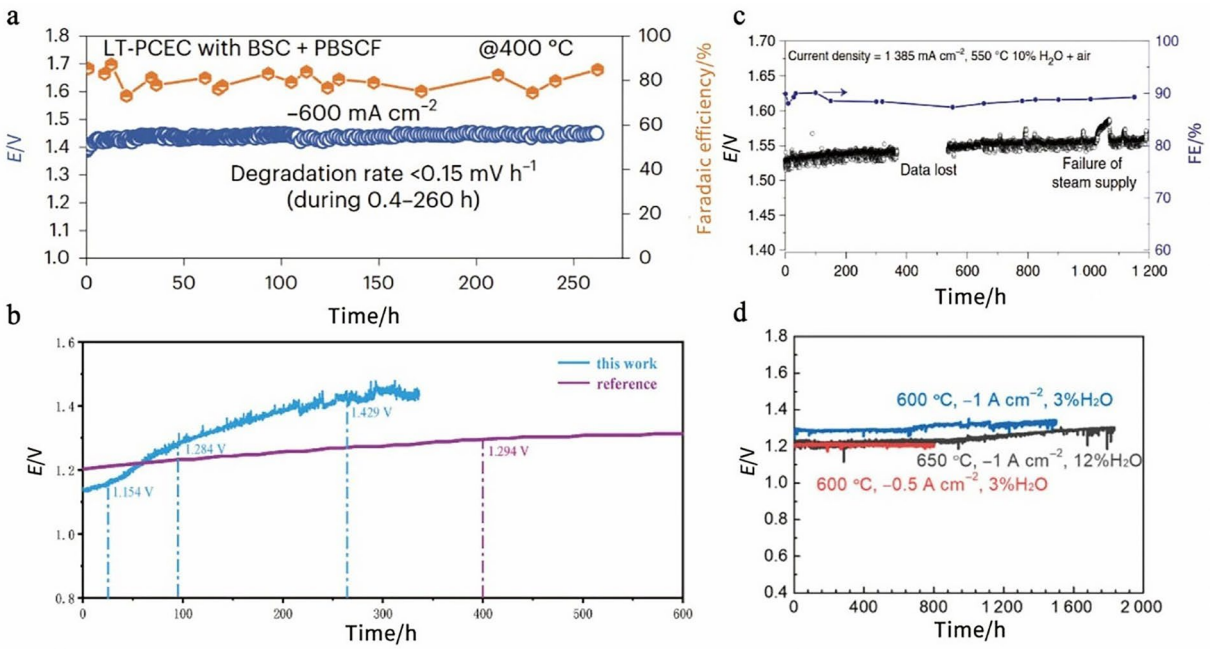

Fig. 9 **a** Long-term stability testing at a current density of 600 mA cm^{-2} at 400 °C. Reprinted with permission from Ref. [60]. Copyright © 2023, Springer Nature. **b** Long-term stability testing at a current density of 2 A cm^{-2} (blue) at 800 °C and 1 A cm^{-2} (purple) at 700 °C. Reprinted with permission from Ref. [115]. Copyright © 2024, Elsevier. **c** Long-term stability testing at a current density of 1385 mA cm^{-2} at 550 °C. Reprinted with permission from Ref. [20]. Copyright © 2019, Springer Nature. **d** Long-term stability testing at a current density of 1.0 A cm^{-2} at 650 °C. Reprinted with permission from Ref. [92]. Copyright © 2021, American Chemical Society

two categories: partial-spectrum coupling and full-spectrum coupling, as depicted in Fig. 6.

5.1 Partial Spectrum Coupling

In SOEC systems, the main methods of utilizing solar energy involve the use of photovoltaics, CSPs, and solar thermal collectors. These methods are used to generate the electrical and thermal energy required for SOECs [116]. Since these devices are capable of absorbing only a portion of the solar spectrum for energy conversion, constructing a system by merely interconnecting these devices leads to the coupling of a partial solar spectrum with SOECs. While this approach is relatively straightforward to implement in practical applications, it does not fully leverage the potential of the entire solar spectrum. Currently, many studies are exploring the integration of SOECs with photovoltaic devices, CSP systems, and other devices or systems, such as thermoelectric generators and energy storage systems [63, 117–119], thereby constructing innovative multigeneration energy systems.

Restrepo et al. introduced an innovative arrangement for hydrogen generation in which an SOEC is operated in the thermoneutral mode. This system is powered by electricity derived from a concentrated photovoltaic array and augmented by thermal energy harvested from a solar field. The design incorporates both tubular and closed volumetric receivers for steam generation and superheating processes, which are complemented by an intricate heat exchange network that efficiently recovers thermal energy at the SOEC outlet. This arrangement achieves a notable hydrogen efficiency of 31.8% [120], as shown in Fig. 10a. Razmi et al. proposed a novel design based on the hybridization of R-SOCs with a high-temperature heliostat solar field, as shown in Fig. 10b. The system comprises four primary units, including a heliostat solar field, an SOEC, an SOFC, and a Kalina cycle system, and has a hydrogen production rate of 7.76 t per day when the SOEC is used and a power generation of 54.3 MWh when the SOFC is used for peak demand shaving [121]. Wang et al. introduced an innovative direct solar irradiated SOEC system, as shown in Fig. 10c. This method not only harnesses solar energy through direct irradiation but also integrates an efficient heat management system to maintain the high-temperature environment required for electrolysis. Under optimal operational parameters, the system achieved a current density of approximately 359 mA cm^{-2} at 1.5 V [122]. Wang et al. presented a novel hybrid hydrogen storage SOEC system powered by both photovoltaic and solar dish collector technologies, as shown in Fig. 10d. This innovative approach also incorporates a molten carbonate fuel cell to efficiently convert stored hydrogen into electricity during periods of

Table 2 Summary of representative SOEC-coupled solar energy systems

Coupling types	Reaction	Operating temperature	Reaction conversion rate/yield	Efficiency	References
Integrated system with solar methane cracking and co-electrolysis	$2H_2O \rightarrow O_2 + 2H_2$ $H_2 + CO_2 \rightarrow CO + H_2O$	800 °C	Methane conversion: 95% H_2 production rate: 5.4 t per day Syngas production rate: 14.8 t per day Methanol production rate: 3.9 t per day	SOEC energy efficiency: 69.3% SOEC exergy efficiency: 29.3% Integrated system energy Efficiency: 40.6% Integrated system exergy efficiency: 37.5%	[63]
Solar-driven SOEC co-electrolysis for renewable methanol	$H_2O + CO_2 \rightarrow CO + H_2 + O_2$ $H_2O + CO \rightarrow CO_2 + H_2$ $3H_2 + CO_2 \rightarrow CH_3OH + H_2O$ $2H_2 + CO \rightarrow CH_3OH$	800 °C	CO_2 conversion: 92.8% (1 073 K) H_2O conversion: 94.7% (1 073 K) Methanol production rate: 46.3 kg h^{-1}	Energy efficiency: 59% Exergy efficiency: 80.9% STF efficiency: 34.50%	[132]
Solar hydrogen generation system integrating photovoltaic panel/photon-enhanced thermionic emission and high-temperature electrolysis cell	$2H_2O \rightarrow O_2 + 2H_2$	600 °C–1 000 °C	No data	First-law thermodynamic efficiency: 77.05% Exergy efficiency: 55.99% Solar-to-hydrogen efficiency: 29.61%	[75]
Integrated solar reactor using SOEC	$2H_2O \rightarrow O_2 + 2H_2$	Ambient temperature: 300 K Gas inlet temperature: 400 K	H_2O conversion ratio: 74.13%	Energy conversion efficiency: 25.58%	[116]
Integrated solar reactor using SOEC	$2H_2O \rightarrow O_2 + 2H_2$	760–920 °C	No data	Energy conversion efficiency: ~ 30%	[133]
Integrated solar reactor using SOEC	$2H_2O \rightarrow O_2 + 2H_2$	Gas outlet temperature: 323.15–353.15 K	H_2 production rate: 0.256 8 kg s^{-1}	Exergy efficiency: 13.15%	[73]
Solar heat integrated SOEC	$2H_2O \rightarrow O_2 + 2H_2$	770 °C	H_2O conversion rate: 70%	Electrical stack efficiency: 93%	[125]

Note: Data are extracted from different resources, thus with different significant digits

peak demand. The system demonstrated a remarkable ability to generate up to 3.9 kg of H_2 per day [123]. Lin et al. introduced an integrated solar-driven high-temperature electrolysis system operating with concentrated irradiation, as shown in Fig. 10e. This advanced concept combines a solar cavity receiver for reactant heating, an SOEC stack for water electrolysis, and concentrated photovoltaic cells to supply the electricity demand of the SOE stack. The system achieves a solar-to-hydrogen (STH) efficiency of up to 19.85% under optimal conditions, with the ability to generate hydrogen at a rate of 3.33% STH efficiency in experimental demonstrations [124]. The integrated design significantly reduces heat losses and enhances the overall performance of the system. Schiller et al. introduced a solar heat integrated solid oxide steam electrolysis system for highly efficient hydrogen production, as shown in Fig. 10f. This system utilizes solar heat for the evaporation and superheating of water, which is then fed into an SOEC stack. The experimental setup includes a solar simulator, a solar steam generator, a steam accumulator, and a 12-cell SOEC stack with approximately 2 kW of electrical power. The system achieved a steam conversion rate of 70% at 93% electrical efficiency, producing 1600 L of H_2 over 4 h of operation [125].

The approach of coupling solar thermoelectric devices with SOECs involves harnessing solar power as the energy input for SOECs, thereby directly substituting the supplied electrical or thermal energy to reduce costs. To further increase the energy density supplied, optical devices such as heliostats and concentrators are employed to focus sunlight effectively. These methods, while improving the system efficiency through external conditions, do not address the intrinsic reaction kinetics or energy barriers. As such, they

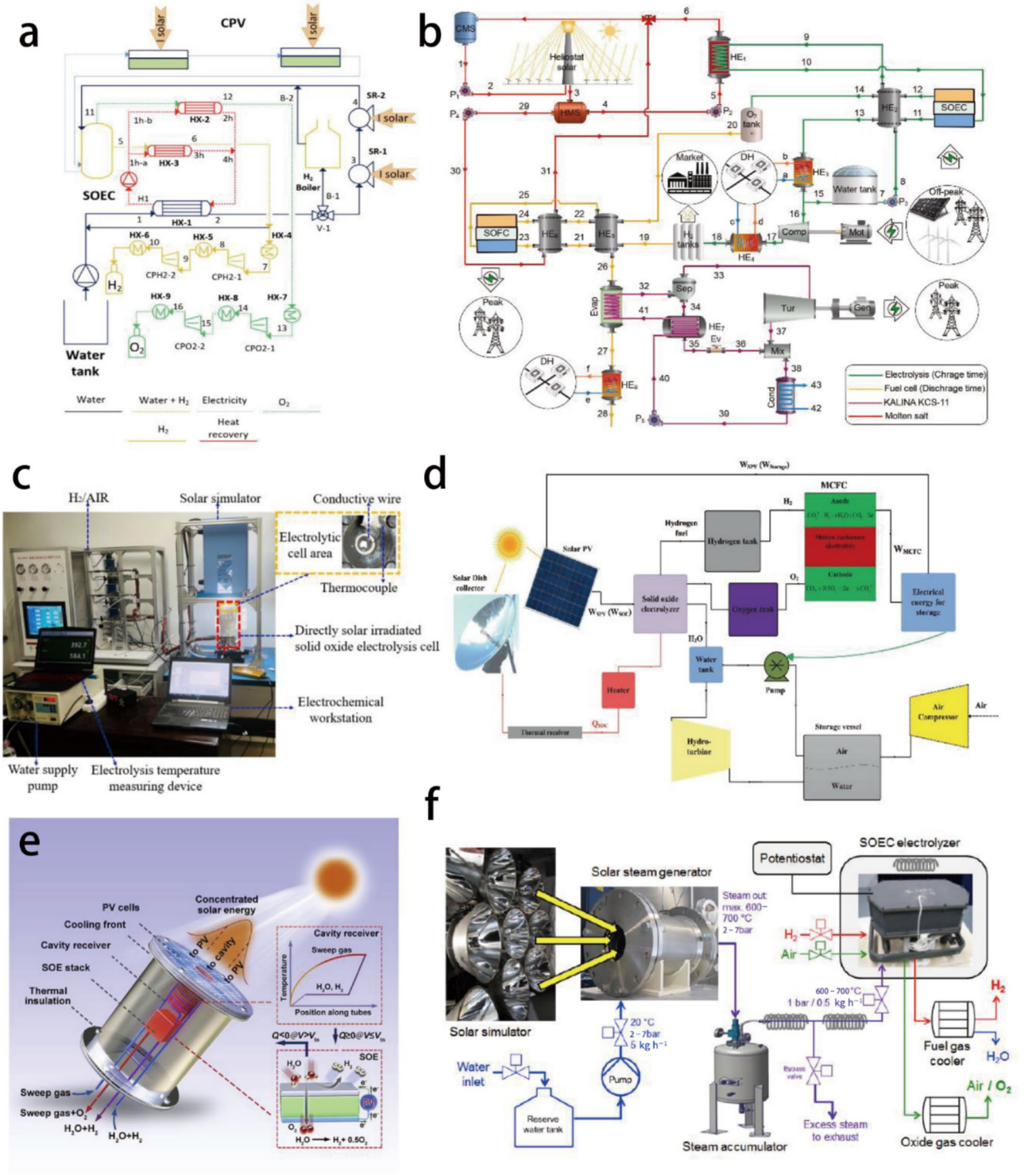

Fig. 10 **a** Schematic of high-temperature solar electrolysis coupled with a thermochemical cycle. Reprinted with permission from Ref. [120]. Copyright © 2022, Elsevier. **b** Schematic of the proposed system based on heliostat solar, SOEC, SOFC, and Kalina cycles for green hydrogen storage. Reprinted with permission from Ref. [121]. Copyright © 2023, Elsevier. **c** Schematic of the direct solar irradiation SOEC system. Reprinted with permission from Ref. [122]. Copyright © 2024, Elsevier. **d** Schematic of the hybrid hydrogen storage SOEC system powered by both photovoltaic and solar dish collector technologies. Reprinted with permission from Ref. [123]. Copyright © 2022, Elsevier. **e** Schematic of an integrated solar-driven high-temperature electrolysis system operating with concentrated irradiation. Reprinted with permission from Ref. [124]. Copyright © 2022, Elsevier. **f** Schematic of a solar heat integrated solid oxide steam electrolysis system (1 bar = 100 kPa). Reprinted with permission from Ref. [125]. Copyright © 2019, Elsevier

do not fully realize the ultimate potential of increasing the overall solar-to-fuel (STF) conversion efficiency.

5.2 Full Spectrum Coupling

The importance of photovoltaics as pivotal elements in coupling solar energy with SOECs for H_2O electrolysis is underscored. However, the conversion of solar energy to electricity by photovoltaic panels is limited to a specific range of wavelengths within the solar spectrum, with the remaining wavelengths inducing a thermal effect [126]. The photovoltaic conversion efficiency rapidly decreases with increasing temperature, which can adversely affect nonthermal processes [127]. When solar energy is converted into thermal energy, energetic photons from the ultraviolet and visible light spectrum, ranging from hundreds to thousands of millielectron volts, are transformed into multiple phonons of much lower energy, leading to significant degradation in energy quality. Thus, in the process of hydrogen production through solar coupling with an SOEC, harnessing the full spectrum of solar energy, including its photothermal-photoelectric potential, is imperative. By synergistically combining the nonthermal and thermal effects, the overall STF conversion efficiency can be substantially enhanced, achieving a more comprehensive utilization of the solar spectrum.

Song et al. introduced an innovative system for hydrogen production that integrates a thermochemical cycle with an SOEC and leverages spectral splitting technology, as shown in Fig. 11a and b. Solar irradiance is meticulously distributed into three distinct bands after concentration and splitting: long-band (λ_1–4 000 nm), short-band (280 nm–λ_2), and medium-band (λ_1–λ_2) light. The medium-band light is absorbed by photovoltaic panels, which efficiently convert it into both electrical energy and thermal energy. The remaining spectral components are then harnessed to propel the two-stage TC process. Preliminary findings indicate that the exergy efficiency of the system can reach approximately 32%, even without incorporating thermal recovery measures. Moreover, the STH conversion efficiency is remarkably high, near 40% [128]. Shafiei Kaleibari et al. simulated a concentrating solar tower plant that incorporates quantum and thermal receivers, as shown in Fig. 11c. These receivers are designed to capture and utilize both thermal energy and electrical energy efficiently through the use of beam splitters. Additionally, dichroic reflectors are employed to effectively divide the incoming solar spectrum. The calculated efficiency of this comprehensive system is 36.5%, which corresponds to H_2 production of 850 g h^{-1} under typical operating conditions [129]. Deng et al. reported a beneficial light-healing effect when light was directly added to the system used to electrolyze H_2O with an SOEC, as shown in Fig. 11d. The light not only prevented the cells from breaking down but also increased the amount of hydrogen produced. They also suggested that the use of light might reduce the loss of oxygen vacancies in the cell material and inhibit excess oxygen formation in the cell structure. More oxygen vacancies could improve electrical conductivity and catalytic activity, enhancing the performance of the SOEC [130]. The light-healing effect might address the current challenge of the poor SOEC stability at high temperatures. Wang et al. proposed an innovative hydrogen generation system that integrates a photovoltaic cell with a photon-enhanced thermionic emission (PETE) cell and an SOEC, as shown in Fig. 11e. The PETE cell unifies photovoltaic and thermionic mechanisms into a single, cohesive physical process. It exploits the high energy per photon and thermal energy derived from thermalization and absorption losses, enhancing overall system efficiency and offering a novel approach to hydrogen production [75]. Deng et al. also introduced a novel solid oxide photoelectrolysis cell (SOPC) for solar-driven hydrogen production [131], as shown in Fig. 11f. This device incorporates a photoresponsive electrode into an SOEC, significantly enhancing performance under light illumination. Notably, they observed the photocurrent in SOPC for the first time and elucidated the photocurrent generation mechanism. The SOPC demonstrates the practicality of substituting solar energy for a portion of electrical energy in hydrogen production, paving the way for sustainable and efficient solutions.

Compared with SOEC systems without spectral splitting, the utilization of the full solar spectrum offers several advantages, such as increased energy utilization efficiency, minimized energy dissipation, and the potential to directly drive chemical reactions, thereby converting solar energy into chemical energy more effectively. However, current research on the coupling of solar spectral splitting with SOECs is limited, and there are potential limitations that need to be addressed. These include the complexity of integrating multiple energy conversion processes, the technological challenges associated with achieving high efficiency across the full solar spectrum, and the economic viability of systems. There is a pressing need for expanded investigations and explorations in this domain to unlock the full potential of this synergistic approach, ensuring that it can be effectively implemented and scaled up for practical applications.

6 Conclusion and Outlook

In the future, the advancement of SOECs for solar energy conversion can be steered in several pivotal directions.

1. Energy conversion efficiency enhancement and coupling method optimization

As innovative energy conversion devices, exploring the optimal coupling methods of SOECs with solar energy is

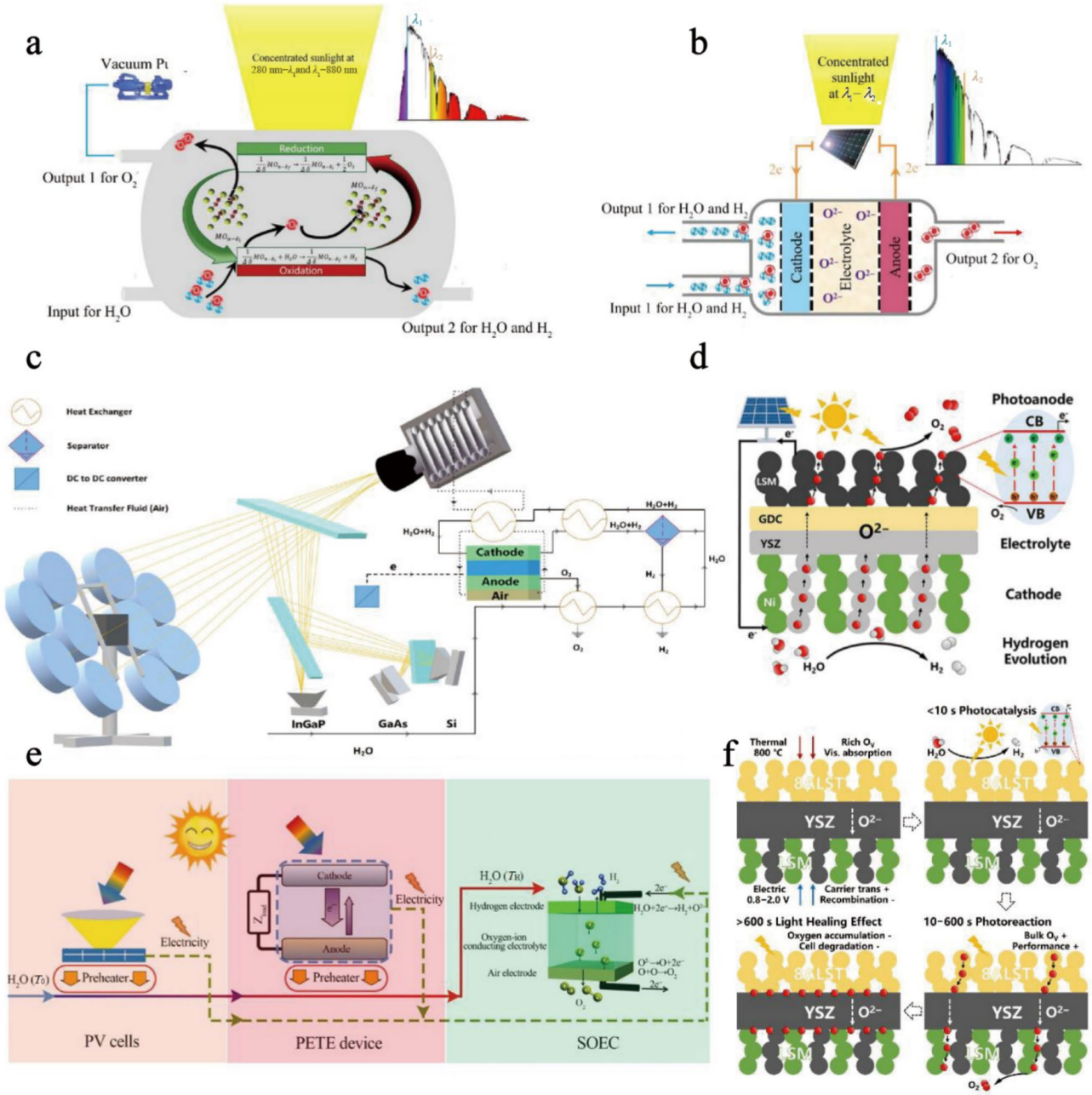

Fig. 11 **a**, **b** Schematic of spectral splitting. Reprinted with permission from Ref. [128]. Copyright © 2023, Elsevier. **c** Schematic of the integrated spectrally split concentrated photovoltaics of an SOEC. Reprinted with permission from Ref. [129]. Copyright © 2019, Elsevier. **d** Mechanistic schematic of a solar driven SOEC. Reprinted with permission from Ref. [130]. Copyright © 2024, American Chemical Society. **e** Schematic of a solar photovoltaic/PETE-SOEC hydrogen production system. Reprinted with permission from Ref. [75]. Copyright © 2020, Elsevier. **f** Schematic of a novel solid oxide photoelectrolysis cell. Reprinted with permission from Ref. [131]. Copyright © 2025, Elsevier

crucial for maximizing energy conversion efficiency. More efforts should be devoted to capitalizing on both thermal and nonthermal solar effects for full-spectrum utilization, directly transforming electrical and thermal energy into targeted chemical energy, circumventing transformations into undesired chemical energy forms, and minimizing energy waste.

2. Development of composite-conductivity and photoresponsive materials

Crafting materials with composite-conductivity for SOECs is essential for facilitating the conduction of electrons, ions, and protons, thereby broadening the reaction interfaces and increasing the number of active sites for

chemical transformation. To broaden industrial applications of SOECs, enhancing their long-term stability under high current densities is equally critical. This can be achieved by developing electrode materials that exhibit photoresponsive properties, leveraging the light-healing effect to prolong operational longevity.

3. Low-temperature operation of solar-driven SOECs

Temperature reduction facilitates deeper integration of SOEC systems with industrial waste heat and solar concentration technologies. However, lower temperatures can lead to rapid declines in electrolyte conductivity, significantly impacting SOEC performance. The development of electrolyte materials capable of providing superior conductivity at lower temperatures is urgently needed.

4. Industrial scale-up and economic viability of solar-driven SOECs

The transition from modest laboratory prototypes to robust industrial-scale systems poses a formidable challenge for solar energy-based SOECs. The majority of SOECs are confined to the experimental stage, with many systematization efforts limited to software simulations. The small scale of SOECs, which seldom exceeds 5 cm^2, highlights the gap between current capabilities and industrial aspirations. Furthermore, the comparatively high costs of SOECs represent a significant barrier to their widespread adoption, particularly compared with other fuel synthesis methods. Future initiatives must focus on devising cost-reduction strategies for the manufacturing of SOECs to increase their market competitiveness.

Acknowledgements This work was financially supported by the National Natural Science Foundation of China (Grant No. 52341602), the Zhejiang Provincial Natural Science Foundation of China under Grant No. LQ24E060001 and Grant No. LDT23E06014E06, Fundamental Research Funds for the Central Universities (Grant No. 2022ZFJH04). This research was also supported by funding from the Canada First Research Excellence Fund (CFREF-2015-00001) as part of the University of Alberta's Future Energy Systems research initiative (FES-T02-P03). The authors gratefully acknowledge this support.

Ethics declarations

Conflict of interest Jing-Li Luo is an editorial board member for *Electrochemical Energy Reviews* and was not involved in the editorial review or the decision to publish this article. All authors declare that there are no competing interests.

References

1. Gaikwad, P.S., Mondal, K., Shin, Y.K., et al.: Enhancing the Faradaic efficiency of solid oxide electrolysis cells: progress and perspective. npj Comput. Mater. **9**, 149 (2023). https://doi.org/10.1038/s41524-023-01044-1
2. Gao, F.Y., Yu, P.C., Gao, M.R.: Seawater electrolysis technologies for green hydrogen production: challenges and opportunities. Curr. Opin. Chem. Eng. **36**, 100827 (2022). https://doi.org/10.1016/j.coche.2022.100827
3. Zhou, Y., Li, R., Lv, Z., et al.: Green hydrogen: a promising way to the carbon-free society. Chin. J. Chem. Eng. **43**, 2–13 (2022). https://doi.org/10.1016/j.cjche.2022.02.001
4. Zang, Y., Wei, P., Li, H., et al.: Catalyst design for electrolytic CO_2 reduction toward low-carbon fuels and chemicals. Electrochem. Energy Rev. **5**, 29 (2022). https://doi.org/10.1007/s41918-022-00140-y
5. Liu, F., Fang, L., Diercks, D., et al.: Rationally designed negative electrode for selective CO_2-to-CO conversion in protonic ceramic electrochemical cells. Nano Energy **102**, 107722 (2022). https://doi.org/10.1016/j.nanoen.2022.107722
6. Kou, Z., Li, X., Wang, T., et al.: Fundamentals, on-going advances and challenges of electrochemical carbon dioxide reduction. Electrochem. Energy Rev. **5**, 82–111 (2022). https://doi.org/10.1007/s41918-021-00096-5
7. Ding, S., Li, M., Pang, W., et al.: A-site deficient perovskite with nano-socketed Ni-Fe alloy particles as highly active and durable catalyst for high-temperature CO_2 electrolysis. Electrochim. Acta **335**, 135683 (2020). https://doi.org/10.1016/j.electacta.2020.135683
8. Lv, X.W., Tian, W.W., Yuan, Z.Y.: Recent advances in high-efficiency electrocatalytic water splitting systems. Electrochem. Energy Rev. **6**, 23 (2023). https://doi.org/10.1007/s41918-022-00159-1
9. Duan, N., Gao, M., Hua, B., et al.: Exploring $Ni(Mn_{1/3}Cr_{2/3})_2O_4$ spinel-based electrodes for solid oxide cells. J. Mater. Chem. A **8**, 3988–3998 (2020). https://doi.org/10.1039/c9ta11878k
10. Li, M., Hua, B., Chen, J., et al.: Charge transfer dynamics in RuO_2/perovskite nanohybrid for enhanced electrocatalysis in solid oxide electrolyzers. Nano Energy **57**, 186–194 (2019). https://doi.org/10.1016/j.nanoen.2018.12.048
11. Wang, W., Gan, L., Lemmon, J.P., et al.: Enhanced carbon dioxide electrolysis at redox manipulated interfaces. Nat. Commun. **10**, 1550 (2019). https://doi.org/10.1038/s41467-019-09568-1
12. Samavati, M., Santarelli, M., Martin, A., et al.: Thermodynamic and economy analysis of solid oxide electrolyser system for syngas production. Energy **122**, 37–49 (2017). https://doi.org/10.1016/j.energy.2017.01.067
13. Ye, Y., Lee, W., Pan, J., et al.: Tuning the product selectivity of CO_2/H_2O co-electrolysis using CeO_2-modified proton-conducting electrolysis cells. Energy Environ. Sci. **16**, 3137–3145 (2023). https://doi.org/10.1039/d3ee01468a
14. Pan, Z., Duan, C., Pritchard, T., et al.: High-yield electrochemical upgrading of CO_2 into CH_4 using large-area protonic ceramic

electrolysis cells. Appl. Catal. B Environ. Energy **307**, 121196 (2022). https://doi.org/10.1016/j.apcatb.2022.121196
15. Zhu, C., Hou, S., Hu, X., et al.: Electrochemical conversion of methane to ethylene in a solid oxide electrolyzer. Nat. Commun. **10**, 1173 (2019). https://doi.org/10.1038/s41467-019-09083-3
16. Xi, X., Liu, J., Fan, Y., et al.: Reducing d-p band coupling to enhance CO_2 electrocatalytic activity by Mg-doping in $Sr_2FeMoO_{6-\delta}$ double perovskite for high performance solid oxide electrolysis cells. Nano Energy **82**, 105707 (2021). https://doi.org/10.1016/j.nanoen.2020.105707
17. Patcharavorachot, Y., Chatrattanawet, N., Arpornwichanop, A., et al.: Comparative energy, economic, and environmental analyses of power-to-gas systems integrating SOECs in steam-electrolysis and co-electrolysis and methanation. Therm. Sci. Eng. Prog. **42**, 101873 (2023). https://doi.org/10.1016/j.tsep.2023.101873
18. Gao, R., Zhang, L., Wang, L., et al.: Efficient utilization of CO_2 in power-to-liquids/power-to-gas hybrid processes: an economic-environmental assessment. J. CO2 Util. **68**, 102376 (2023). https://doi.org/10.1016/j.jcou.2022.102376
19. Du, N., Roy, C., Peach, R., et al.: Anion-exchange membrane water electrolyzers. Chem. Rev. **122**, 11830–11895 (2022). https://doi.org/10.1021/acs.chemrev.1c00854
20. Duan, C., Kee, R., Zhu, H., et al.: Highly efficient reversible protonic ceramic electrochemical cells for power generation and fuel production. Nat. Energy **4**, 230–240 (2019). https://doi.org/10.1038/s41560-019-0333-2
21. Zhu, L., Cadigan, C., Duan, C., et al.: Ammonia-fed reversible protonic ceramic fuel cells with Ru-based catalyst. Commun. Chem. **4**, 121 (2021). https://doi.org/10.1038/s42004-021-00559-2
22. Shimada, H., Yamaguchi, T., Kishimoto, H., et al.: Nanocomposite electrodes for high current density over 3 A cm^{-2} in solid oxide electrolysis cells. Nat. Commun. **10**, 5432 (2019). https://doi.org/10.1038/s41467-019-13426-5
23. Kim, Y.M., Kim, S., Choi, J.: Adiabatic compressed air energy storage system combined with solid-oxide electrolysis cells. Energy Rep. **11**, 1135–1146 (2024). https://doi.org/10.1016/j.egyr.2023.12.070
24. Baxter, S.J., Rine, M., Min, B., et al.: Near 100% CO_2 conversion and CH_4 selectivity in a solid oxide electrolysis cell with integrated catalyst operating at 450 °C. J. CO_2 Util. **59**, 101954 (2022). https://doi.org/10.1016/j.jcou.2022.101954
25. Zheng, Y., Chen, Z., Zhang, J.: Solid oxide electrolysis of H_2O and CO_2 to produce hydrogen and low-carbon fuels. Electrochem. Energy Rev. **4**, 508–517 (2021). https://doi.org/10.1007/s41918-021-00097-4
26. Liu, F., Ding, D., Duan, C.: Protonic ceramic electrochemical cells for synthesizing sustainable chemicals and fuels. Adv. Sci. **10**, 2206478 (2023). https://doi.org/10.1002/advs.202206478
27. Krammer, A., Medved, A., Peham, M., et al.: Dual pressure level methanation of Co-SOEC syngas. Energy Technol. **9**, 2000746 (2021). https://doi.org/10.1002/ente.202000746
28. Li, Z., Li, M., Zhu, Z.: Perovskite cathode materials for low-temperature solid oxide fuel cells: fundamentals to optimization. Electrochem. Energy Rev. **5**, 263–311 (2022). https://doi.org/10.1007/s41918-021-00098-3
29. Si, F., Liu, S., Liang, Y., et al.: Fuel cell reactors for the clean cogeneration of electrical energy and value-added chemicals. Electrochem. Energy Rev. **5**, 25 (2022). https://doi.org/10.1007/s41918-022-00168-0
30. Biswas, S., Kaur, G., Giddey, S.: Steam electrolysis in solid oxide electrolytic cells using a cermet of copper and gadolinia doped ceria cathode. Electrochim. Acta **468**, 143150 (2023). https://doi.org/10.1016/j.electacta.2023.143150
31. Zhao, G., Kraglund, M.R., Frandsen, H.L., et al.: Life cycle assessment of H_2O electrolysis technologies. Int. J. Hydrog. Energy **45**, 23765–23781 (2020). https://doi.org/10.1016/j.ijhydene.2020.05.282
32. Vøllestad, E., Strandbakke, R., Tarach, M., et al.: Mixed proton and electron conducting double perovskite anodes for stable and efficient tubular proton ceramic electrolysers. Nat. Mater. **18**, 752–759 (2019). https://doi.org/10.1038/s41563-019-0388-2
33. Pei, K., Zhou, Y., Xu, K., et al.: Surface restructuring of a perovskite-type air electrode for reversible protonic ceramic electrochemical cells. Nat. Commun. **13**, 2207 (2022). https://doi.org/10.1038/s41467-022-29866-5
34. Zhao, Y., Niu, Z., Zhao, J., et al.: Recent advancements in photoelectrochemical water splitting for hydrogen production. Electrochem. Energy Rev. **6**, 14 (2023). https://doi.org/10.1007/s41918-022-00153-7
35. Jolaoso, L.A., Duan, C., Kazempoor, P.: Life cycle analysis of a hydrogen production system based on solid oxide electrolysis cells integrated with different energy and wastewater sources. Int. J. Hydrog. Energy **52**, 485–501 (2024). https://doi.org/10.1016/j.ijhydene.2023.07.129
36. Malavasi, L., Fisher, C.A.J., Islam, M.S.: Oxide-ion and proton conducting electrolyte materials for clean energy applications: structural and mechanistic features. Chem. Soc. Rev. **39**, 4370 (2010). https://doi.org/10.1039/b915141a
37. Hauch, A., Küngas, R., Blennow, P., et al.: Recent advances in solid oxide cell technology for electrolysis. Science **370**, eaba6118 (2020). https://doi.org/10.1126/science.aba6118
38. Ravi Kumar, K., Krishna Chaitanya, N.V.V., Sendhil Kumar, N.: Solar thermal energy technologies and its applications for process heating and power generation: a review. J. Clean. Prod. **282**, 125296 (2021). https://doi.org/10.1016/j.jclepro.2020.125296
39. Hong, J., Xu, C., Deng, B., et al.: Photothermal chemistry based on solar energy: from synergistic effects to practical applications. Adv. Sci. **9**, 2103926 (2022). https://doi.org/10.1002/advs.202103926
40. Takata, T., Jiang, J., Sakata, Y., et al.: Photocatalytic water splitting with a quantum efficiency of almost unity. Nature **581**, 411–414 (2020). https://doi.org/10.1038/s41586-020-2278-9
41. Yang, S., Chen, S., Mosconi, E., et al.: Stabilizing halide perovskite surfaces for solar cell operation with wide-bandgap lead oxysalts. Science **365**, 473–478 (2019). https://doi.org/10.1126/science.aax3294
42. Li, R., Takata, T., Zhang, B., et al.: Criteria for efficient photocatalytic water splitting revealed by studying carrier dynamics in a model Al-doped $SrTiO_3$ photocatalyst. Angew. Chem. Int. Ed. **62**, e202313537 (2023). https://doi.org/10.1002/anie.202313537
43. Li, W., Luo, J.L.: High-temperature electrochemical devices based on dense ceramic membranes for CO_2 conversion and utilization. Electrochem. Energy Rev. **4**, 518–544 (2021). https://doi.org/10.1007/s41918-021-00099-2
44. Saqib, M., Choi, I.G., Bae, H., et al.: Transition from perovskite to misfit-layered structure materials: a highly oxygen deficient and stable oxygen electrode catalyst. Energy Environ. Sci. **14**, 2472–2484 (2021). https://doi.org/10.1039/d0ee02799e
45. Zhu, B., Fan, L., Mushtaq, N., et al.: Semiconductor electrochemistry for clean energy conversion and storage. Electrochem. Energy Rev. **4**, 757–792 (2021). https://doi.org/10.1007/s41918-021-00112-8
46. Irvine, J.T.S., Neagu, D., Verbraeken, M.C., et al.: Evolution of the electrochemical interface in high-temperature fuel cells and electrolysers. Nat. Energy **1**, 15014 (2016). https://doi.org/10.1038/nenergy.2015.14
47. Ding, H., Wu, W., Jiang, C., et al.: Self-sustainable protonic ceramic electrochemical cells using a triple conducting electrode for hydrogen and power production. Nat. Commun. **11**, 1907 (2020). https://doi.org/10.1038/s41467-020-15677-z

48. Zhang, J., Shi, Y., Cai, N.: An approximate analytical model of reduction of carbon dioxide in solid oxide electrolysis cell by regular and singular perturbation methods. Electrochim. Acta **139**, 190–200 (2014). https://doi.org/10.1016/j.electacta.2014.07.026
49. Ji, H.I., Lee, J.H., Son, J.W., et al.: Protonic ceramic electrolysis cells for fuel production: a brief review. J. Korean Ceram. Soc. **57**, 480–494 (2020). https://doi.org/10.1007/s43207-020-00059-4
50. Yu, J., Men, H.J., Qu, Y.M., et al.: Performance of Ni-Fe bimetal based cathode for intermediate temperature solid oxide electrolysis cell. Solid State Ion. **346**, 115203 (2020). https://doi.org/10.1016/j.ssi.2019.115203
51. Li, M., Hou, J., Fan, Y., et al.: Interface modification of Ru-CeO_2 co-infiltrated SFM electrode and construction of SDC/YSZ bilayer electrolyte for direct CO_2 electrolysis. Electrochim. Acta **426**, 140771 (2022). https://doi.org/10.1016/j.electacta.2022.140771
52. Hou, J., Wang, Q., Li, J., et al.: Rational design of an in situ co-assembly nanocomposite cathode $La_{0.5}Sr_{1.5}MnO_{4+\delta}$-$La_{0.5}Sr_{0.5}MnO_{3-\delta}$ for lower-temperature proton-conducting solid oxide fuel cells. J. Power Sources **466**, 228240 (2020). https://doi.org/10.1016/j.jpowsour.2020.228240
53. Xi, X., Liu, J., Luo, W., et al.: Unraveling the enhanced kinetics of $Sr_2Fe_{1+x}Mo_{1-x}O_{6-\delta}$ electrocatalysts for high-performance solid oxide cells. Adv. Energy Mater. **11**, 2102845 (2021). https://doi.org/10.1002/aenm.202102845
54. Jiang, S.P.: Solid-state electrochemistry and solid oxide fuel cells: status and future prospects. Electrochem. Energy Rev. **5**, 21 (2022). https://doi.org/10.1007/s41918-022-00160-8
55. Duan, N., Yang, J., Gao, M., et al.: Multi-functionalities enabled fivefold applications of $LaCo_{0.6}Ni_{0.4}O_{3-\delta}$ in intermediate temperature symmetrical solid oxide fuel/electrolysis cells. Nano Energy **77**, 105207 (2020). https://doi.org/10.1016/j.nanoen.2020.105207
56. Kwon, O.H., Choi, G.M.: Electrical conductivity of thick film YSZ. Solid State Ion. **177**, 3057–3062 (2006). https://doi.org/10.1016/j.ssi.2006.07.039
57. Bi, L., Boulfrad, S., Traversa, E.: Steam electrolysis by solid oxide electrolysis cells (SOECs) with proton-conducting oxides. Chem. Soc. Rev. **43**, 8255–8270 (2014). https://doi.org/10.1039/c4cs00194j
58. Lv, Z., Chen, G., Wei, K., et al.: Preparation and performance evaluation of low temperature SOEC using lithium compounds as electrodes. Int. J. Hydrog. Energy **55**, 386–393 (2024). https://doi.org/10.1016/j.ijhydene.2023.11.238
59. Kim, D., Bae, K.T., Kim, K.J., et al.: High-performance protonic ceramic electrochemical cells. ACS Energy Lett. **7**, 2393–2400 (2022). https://doi.org/10.1021/acsenergylett.2c01370
60. Liu, F., Deng, H., Diercks, D., et al.: Lowering the operating temperature of protonic ceramic electrochemical cells to < 450 °C. Nat. Energy **8**, 1145–1157 (2023). https://doi.org/10.1038/s41560-023-01350-4
61. Duan, C., Tong, J., Shang, M., et al.: Readily processed protonic ceramic fuel cells with high performance at low temperatures. Science **349**, 1321–1326 (2015). https://doi.org/10.1126/science.aab3987
62. Fan, Y., Xi, X., Medvedev, D., et al.: Emerging anode materials architectured with NiCoFe ternary alloy nanoparticles for ethane-fueled protonic ceramic fuel cells. J. Power Sources **515**, 230634 (2021). https://doi.org/10.1016/j.jpowsour.2021.230634
63. Banu, A., Bicer, Y.: Energy and exergy analysis of an integrated system with solar methane cracking and co-electrolysis of CO_2/H_2O for efficient carbon management. Int. J. Hydrog. Energy **52**, 580–593 (2024). https://doi.org/10.1016/j.ijhydene.2023.09.163
64. Wang, Y., Du, Y., Ni, M., et al.: Three-dimensional modeling of flow field optimization for co-electrolysis solid oxide electrolysis cell. Appl. Therm. Eng. **172**, 114959 (2020). https://doi.org/10.1016/j.applthermaleng.2020.114959
65. Liu, Z., Bai, Y., Sun, H., et al.: Synergistic dual-phase air electrode enables high and durable performance of reversible proton ceramic electrochemical cells. Nat. Commun. **15**, 472 (2024). https://doi.org/10.1038/s41467-024-44767-5
66. Chen, Y., Wu, X., Hu, H., et al.: System level performance analysis and parameter optimization of hydrogen production based on solid oxide electrolytic cell. Appl. Energy **347**, 121329 (2023). https://doi.org/10.1016/j.apenergy.2023.121329
67. Lu, B., Zhang, Z., Zhang, Z., et al.: Control strategy of solid oxide electrolysis cell operating temperature under real fluctuating renewable power. Energy Convers. Manag. **299**, 117852 (2024). https://doi.org/10.1016/j.enconman.2023.117852
68. Ni, M., Leung, M., Leung, D.: Parametric study of solid oxide steam electrolyzer for hydrogen production. Int. J. Hydrog. Energy **32**, 2305–2313 (2007). https://doi.org/10.1016/j.ijhydene.2007.03.001
69. Fei, Y., Li, A., Zhang, C., et al.: Performance optimization of solid oxide electrolysis cell for syngas production by high temperature co-electrolysis via differential evolution algorithm with practical constraints. Energy Conv. Manag. **300**, 117911 (2024). https://doi.org/10.1016/j.enconman.2023.117911
70. Wang, F., Wang, L., Ou, Y., et al.: Thermodynamic analysis of solid oxide electrolyzer integration with engine waste heat recovery for hydrogen production. Case Stud. Therm. Eng. **27**, 101240 (2021). https://doi.org/10.1016/j.csite.2021.101240
71. Lang, M., Raab, S., Lemcke, M.S., et al.: Long-term behavior of a solid oxide electrolyzer (SOEC) stack. Fuel Cells **20**, 690–700 (2020). https://doi.org/10.1002/fuce.201900245
72. Ni, M.: Modeling of a solid oxide electrolysis cell for carbon dioxide electrolysis. Chem. Eng. J. **164**, 246–254 (2010). https://doi.org/10.1016/j.cej.2010.08.032
73. Mohebali Nejadian, M., Ahmadi, P., Houshfar, E.: Comparative optimization study of three novel integrated hydrogen production systems with SOEC, PEM, and alkaline electrolyzer. Fuel **336**, 126835 (2023). https://doi.org/10.1016/j.fuel.2022.126835
74. Mohammadi, A., Mehrpooya, M.: Techno-economic analysis of hydrogen production by solid oxide electrolyzer coupled with dish collector. Energy Conv. Manag. **173**, 167–178 (2018). https://doi.org/10.1016/j.enconman.2018.07.073
75. Wang, H., Kong, H., Pu, Z., et al.: Feasibility of high efficient solar hydrogen generation system integrating photovoltaic cell/photon-enhanced thermionic emission and high-temperature electrolysis cell. Energy Convers. Manag. **210**, 112699 (2020). https://doi.org/10.1016/j.enconman.2020.112699
76. Ebbesen, S.D., Mogensen, M.: Electrolysis of carbon dioxide in solid oxide electrolysis cells. J. Power Sources **193**, 349–358 (2009). https://doi.org/10.1016/j.jpowsour.2009.02.093
77. Zhou, M., Liu, Z., Yan, X., et al.: Simultaneous electrochemical reduction of carbon dioxide and partial oxidation of methane in a solid oxide cell with silver-based cathode and nickel-based anode. J. Electrochem. Soc. **169**, 034502 (2022). https://doi.org/10.1149/1945-7111/ac554d
78. Xu, H., Ma, J., Tan, P., et al.: Enabling thermal-neutral electrolysis for CO_2-to-fuel conversions with a hybrid deep learning strategy. Energy Convers. Manag. **230**, 113827 (2021). https://doi.org/10.1016/j.enconman.2021.113827
79. Liang, H., Wang, F., Yang, L., et al.: Progress in full spectrum solar energy utilization by spectral beam splitting hybrid PV/T system. Renew. Sustain. Energy Rev. **141**, 110785 (2021). https://doi.org/10.1016/j.rser.2021.110785

80. Liu, Y., Wang, F., Jiao, Z., et al.: Photochemical systems for solar-to-fuel production. Electrochem. Energy Rev. **5**, 5 (2022). https://doi.org/10.1007/s41918-022-00132-y
81. Li, Z., Zhang, H., Xu, H., et al.: Advancing the multiscale understanding on solid oxide electrolysis cells via modelling approaches: a review. Renew. Sustain. Energy Rev. **141**, 110863 (2021). https://doi.org/10.1016/j.rser.2021.110863
82. Tanaka, Y., Hoerlein, M.P., Schiller, G.: Numerical simulation of steam electrolysis with a solid oxide cell for proper evaluation of cell performances. Int. J. Hydrog. Energy **41**, 752–763 (2016). https://doi.org/10.1016/j.ijhydene.2015.11.048
83. Menon, V., Fu, Q., Janardhanan, V.M., et al.: A model-based understanding of solid-oxide electrolysis cells (SOECs) for syngas production by H_2O/CO_2 co-electrolysis. J. Power Sources **274**, 768–781 (2015). https://doi.org/10.1016/j.jpowsour.2014.09.158
84. Li, W., Shi, Y., Luo, Y., et al.: Elementary reaction modeling of solid oxide electrolysis cells: main zones for heterogeneous chemical/electrochemical reactions. J. Power Sources **273**, 1–13 (2015). https://doi.org/10.1016/j.jpowsour.2014.08.120
85. Nerat, M., Juričić, Đ: Modelling of anode delamination in solid oxide electrolysis cell and analysis of its effects on electrochemical performance. Int. J. Hydrog. Energy **43**, 8179–8189 (2018). https://doi.org/10.1016/j.ijhydene.2018.02.189
86. Banerjee, A., Wang, Y., Diercks, J., et al.: Hierarchical modeling of solid oxide cells and stacks producing syngas via H_2O/CO_2 co-electrolysis for industrial applications. Appl. Energy **230**, 996–1013 (2018). https://doi.org/10.1016/j.apenergy.2018.08.122
87. Ba, L., Xiong, X., Lei, Z., et al.: A study on solid oxide electrolyzer stack and system performance based on alternative mapping models. Int. J. Hydrog. Energy **47**, 12469–12486 (2022). https://doi.org/10.1016/j.ijhydene.2022.01.253
88. Hu, T., Zhu, F., Xia, J., et al.: In situ engineering of a cobalt-free perovskite air electrode enabling efficient reversible oxygen reduction/evolution reactions. Adv. Funct. Mater. **33**, 2305567 (2023). https://doi.org/10.1002/adfm.202305567
89. Luo, Z., Zhou, Y., Hu, X., et al.: Highly conductive and durable Nb(Ta)-doped proton conductors for reversible solid oxide cells. ACS Energy Lett. **7**, 2970–2978 (2022). https://doi.org/10.1021/acsenergylett.2c01544
90. Murphy, R., Zhou, Y., Zhang, L., et al.: A new family of proton-conducting electrolytes for reversible solid oxide cells: $BaHf_xCe_{0.8-x}Y_{0.1}Yb_{0.1}O_{3-\delta}$. Adv. Funct. Mater. **30**, 2002265 (2020). https://doi.org/10.1002/adfm.202002265
91. Yun, B.H., Kim, K.J., Joh, D.W., et al.: Highly active and durable double-doped bismuth oxide-based oxygen electrodes for reversible solid oxide cells at reduced temperatures. J. Mater. Chem. A **7**, 20558–20566 (2019). https://doi.org/10.1039/c9ta09203j
92. Zhou, Y., Liu, E., Chen, Y., et al.: An active and robust air electrode for reversible protonic ceramic electrochemical cells. ACS Energy Lett. (2021). https://doi.org/10.1021/acsenergylett.1c00432
93. Choi, S., Davenport, T.C., Haile, S.M.: Protonic ceramic electrochemical cells for hydrogen production and electricity generation: exceptional reversibility, stability, and demonstrated faradaic efficiency. Energy Environ. Sci. **12**, 206–215 (2019). https://doi.org/10.1039/c8ee02865f
94. Wu, W., Ding, H., Zhang, Y., et al.: 3D self-architectured steam electrode enabled efficient and durable hydrogen production in a proton-conducting solid oxide electrolysis cell at temperatures lower than 600 °C. Adv. Sci. **5**, 1800360 (2018). https://doi.org/10.1002/advs.201800360
95. Li, W., Guan, B., Ma, L., et al.: High performing triple-conductive $Pr_2NiO_{4+\delta}$ anode for proton-conducting steam solid oxide electrolysis cell. J. Mater. Chem. A **6**, 18057–18066 (2018). https://doi.org/10.1039/c8ta04018d
96. Tang, W., Ding, H., Bian, W., et al.: Understanding of A-site deficiency in layered perovskites: promotion of dual reaction kinetics for water oxidation and oxygen reduction in protonic ceramic electrochemical cells. J. Mater. Chem. A **8**, 14600–14608 (2020). https://doi.org/10.1039/d0ta05137c
97. Tang, C., Akimoto, K., Wang, N., et al.: The effect of an anode functional layer on the steam electrolysis performances of protonic solid oxide cells. J. Mater. Chem. A **9**, 14032–14042 (2021). https://doi.org/10.1039/d1ta02848k
98. Niu, Y., Zhou, Y., Zhang, W., et al.: Highly active and durable air electrodes for reversible protonic ceramic electrochemical cells enabled by an efficient bifunctional catalyst. Adv. Energy Mater. **12**, 2103783 (2022). https://doi.org/10.1002/aenm.202103783
99. Zhu, F., He, F., Liu, D., et al.: A surface reconfiguration of a perovskite air electrode enables an active and durable reversible protonic ceramic electrochemical cell. Energy Storage Mater. **53**, 754–762 (2022). https://doi.org/10.1016/j.ensm.2022.10.009
100. Li, P., Niu, Y., Du, J., et al.: Medium-entropy perovskite $Pr_{0.4}Ba_{0.2}Ca_{0.2}La_{0.2}Co_{0.2}Fe_{0.8}O_3$ as a promising bifunctional electrocatalyst for electrochemical energy conversion device. Chem. Eng. Sci. **293**, 120034 (2024). https://doi.org/10.1016/j.ces.2024.120034
101. Li, C., Deng, Y., Yang, L., et al.: An active and stable hydrogen electrode of solid oxide cells with exsolved Fe-Co-Ni nanoparticles from $Sr_2FeCo_{0.2}Ni_{0.2}Mo_{0.6}O_{6-\delta}$ double-perovskite. Adv. Powder Mater. **2**, 100133 (2023). https://doi.org/10.1016/j.apmate.2023.100133
102. Sun, C., Yang, S., Lu, Y., et al.: Tailoring a micro-nanostructured electrolyte-oxygen electrode interface for proton-conducting reversible solid oxide cells. J. Power Sources **449**, 227498 (2020). https://doi.org/10.1016/j.jpowsour.2019.227498
103. Fang, L., Liu, F., Diercks, D., et al.: Boosting the performance of reversible solid oxide electrochemical cells with a novel hybrid oxygen electrode, $Pr_{1.39}Ba_{0.14}Sr_{0.53}Co_{1.48}Fe_{0.76}O_{6-\delta}$-$Ba_{0.66}Sr_{0.34}CoO_{3-\delta}$. J. Mater. Chem. A **11**, 21251–21262 (2023). https://doi.org/10.1039/d3ta03629d
104. Zhang, S.-L., Wang, H., Lu, M.Y., et al.: Cobalt-substituted $SrTi_{0.3}Fe_{0.7}O_{3-\delta}$: a stable high-performance oxygen electrode material for intermediate-temperature solid oxide electrochemical cells. Energy Environ. Sci. **11**, 1870–1879 (2018). https://doi.org/10.1039/c8ee00449h
105. Bae, K.T., Jeong, I., Kim, D., et al.: Highly active cobalt-free perovskites with Bi doping as bifunctional oxygen electrodes for solid oxide cells. Chem. Eng. J. **461**, 142051 (2023). https://doi.org/10.1016/j.cej.2023.142051
106. Yu, H., Im, H.N., Lee, K.T.: Exceptionally high-performance reversible solid oxide electrochemical cells with ultrathin and defect-free free $Sm_{0.075}Nd_{0.075}Ce_{0.85}O_{2-\delta}$ interlayers. Adv. Funct. Mater. **32**, 2207725 (2022). https://doi.org/10.1002/adfm.202207725
107. Park, J.H., Jung, C.H., Kim, K.J., et al.: Enhancing bifunctional electrocatalytic activities of oxygen electrodes via incorporating highly conductive Sm^{3+} and Nd^{3+} double-doped ceria for reversible solid oxide cells. ACS Appl. Mater. Interfaces **13**, 2496–2506 (2021). https://doi.org/10.1021/acsami.0c17238
108. Kim, J., Im, S., Oh, S.H., et al.: Naturally diffused sintering aid for highly conductive bilayer electrolytes in solid oxide cells. Sci. Adv. **7**, eabj8590 (2021). https://doi.org/10.1126/sciadv.abj8590
109. Li, G., Gou, Y., Cheng, X., et al.: Enhanced electrochemical performance of the Fe-based layered perovskite oxygen electrode for reversible solid oxide cells. ACS Appl. Mater. Interfaces **13**, 34282–34291 (2021). https://doi.org/10.1021/acsami.1c08010
110. Bian, W., Wu, W., Wang, B., et al.: Revitalizing interface in protonic ceramic cells by acid etch. Nature **604**, 479–485 (2022). https://doi.org/10.1038/s41586-022-04457-y

111. An, H., Lee, H.W., Kim, B.K., et al.: A 5 cm × 5 cm protonic ceramic fuel cell with a power density of 1.3 W cm^{-2} at 600 °C. Nat. Energy **3**, 870–875 (2018). https://doi.org/10.1038/s41560-018-0230-0
112. Choi, S., Kucharczyk, C.J., Liang, Y., et al.: Exceptional power density and stability at intermediate temperatures in protonic ceramic fuel cells. Nat. Energy **3**, 202–210 (2018). https://doi.org/10.1038/s41560-017-0085-9
113. Navasa, M., Graves, C., Chatzichristodoulou, C., et al.: A three dimensional multiphysics model of a solid oxide electrochemical cell: a tool for understanding degradation. Int. J. Hydrog. Energy **43**, 11913–11931 (2018). https://doi.org/10.1016/j.ijhydene.2018.04.164
114. Chatzichristodoulou, C., Chen, M., Hendriksen, P.V., et al.: Understanding degradation of solid oxide electrolysis cells through modeling of electrochemical potential profiles. Electrochim. Acta **189**, 265–282 (2016). https://doi.org/10.1016/j.electacta.2015.12.067
115. Shao, Q., Jin, D., Lu, Y., et al.: Performance evolution analysis of solid oxide electrolysis cells operating at high current densities. Int. J. Hydrog. Energy **57**, 709–716 (2024). https://doi.org/10.1016/j.ijhydene.2024.01.096
116. Zhang, Q., Chang, Z., Fu, M., et al.: Thermal and electrochemical performance analysis of an integrated solar SOEC reactor for hydrogen production. Appl. Therm. Eng. **229**, 120603 (2023). https://doi.org/10.1016/j.applthermaleng.2023.120603
117. Mohammadpour, M., Houshfar, E., Ashjaee, M.: Performance evaluation and multi-objective optimization of an innovative solar-assisted multigeneration energy storage system for freshwater/O_2/H_2 generation. Sustain. Energy Technol. Assess. **53**, 102755 (2022). https://doi.org/10.1016/j.seta.2022.102755
118. Ghaebi, H., Ahmadi, S.: Energy and exergy evaluation of an innovative hybrid system coupled with HRSG and HDH desalination units. J. Clean. Prod. **252**, 119821 (2020). https://doi.org/10.1016/j.jclepro.2019.119821
119. Roy, D., Samanta, S.: A solar-assisted power-to-hydrogen system based on proton-conducting solid oxide electrolyzer cells. Renew. Energy **220**, 119562 (2024). https://doi.org/10.1016/j.renene.2023.119562
120. Restrepo, J.C., Luis Izidoro, D., Milena Lozano Násner, A., et al.: Techno-economical evaluation of renewable hydrogen production through concentrated solar energy. Energy Conv. Manag. **258**, 115372 (2022). https://doi.org/10.1016/j.enconman.2022.115372
121. Razmi, A.R., Hanifi, A.R., Shahbakhti, M.: Design, thermodynamic, and economic analyses of a green hydrogen storage concept based on solid oxide electrolyzer/fuel cells and heliostat solar field. Renew. Energy **215**, 118996 (2023). https://doi.org/10.1016/j.renene.2023.118996
122. Wang, H., Guan, C., Lu, Y., et al.: Investigation into the electrolysis performance of a novel directly solar irradiated solid oxide electrolysis cell. Chem. Eng. J. **499**, 156255 (2024). https://doi.org/10.1016/j.cej.2024.156255
123. Wang, S., Wu, X., Jafarmadar, S., et al.: Numerical assessment of a hybrid energy system based on solid oxide electrolyzer, solar energy and molten carbonate fuel cell for the generation of electrical energy and hydrogen fuel with electricity storage option. J. Energy Storage **54**, 105274 (2022). https://doi.org/10.1016/j.est.2022.105274
124. Lin, M., Suter, C., Diethelm, S., et al.: Integrated solar-driven high-temperature electrolysis operating with concentrated irradiation. Joule **6**, 2102–2121 (2022). https://doi.org/10.1016/j.joule.2022.07.013
125. Schiller, G., Lang, M., Szabo, P., et al.: Solar heat integrated solid oxide steam electrolysis for highly efficient hydrogen production. J. Power Sources **416**, 72–78 (2019). https://doi.org/10.1016/j.jpowsour.2019.01.059
126. Cheknane, A., Hilal, H.S., Charles, J.P., et al.: Modelling and simulation of InGaP solar cells under solar concentration: series resistance measurement and prediction. Solid State Sci. **8**, 556–559 (2006). https://doi.org/10.1016/j.solidstatesciences.2006.01.001
127. Wang, Y., Liu, Q., Lei, J., et al.: A three-dimensional simulation of a parabolic trough solar collector system using molten salt as heat transfer fluid. Appl. Therm. Eng. **70**, 462–476 (2014). https://doi.org/10.1016/j.applthermaleng.2014.05.051
128. Song, H., Wang, H., Zheng, H., et al.: Analysis of cascade and hybrid processes for hydrogen production by full spectrum solar energy utilization. Energy Conv. Manag. **291**, 117289 (2023). https://doi.org/10.1016/j.enconman.2023.117289
129. Shafiei Kaleibari, S., Yanping, Z., Abanades, S.: Solar-driven high temperature hydrogen production via integrated spectrally split concentrated photovoltaics (SSCPV) and solar power tower. Int. J. Hydrog. Energy **44**, 2519–2532 (2019). https://doi.org/10.1016/j.ijhydene.2018.12.039
130. Deng, G., Mei, J., Xie, Y., et al.: Photoinduced mitigation of solid oxide electrolysis cell degradation: light healing effect on oxygen vacancies. ACS Appl. Energy Mater. **7**, 373–379 (2024). https://doi.org/10.1021/acsaem.3c02754
131. Deng, G., Xu, C., Mei, J., et al.: A novel solid oxide photoelectrolysis cell for solar-driven hydrogen production. Chem. Eng. J. **504**, 158794 (2025). https://doi.org/10.1016/j.cej.2024.158794
132. Khan, M.S., Lin, Z., Lin, L., et al.: Techno-economic analysis of solar-driven co-electrolysis for renewable methanol production using SOEC. Energy Conv. Manag. **302**, 118129 (2024). https://doi.org/10.1016/j.enconman.2024.118129
133. Zhang, Q., Chang, Z., Fu, M., et al.: Thermal performance analysis of an integrated solar reactor using solid oxide electrolysis cells (SOEC) for hydrogen production. Energy Conv. Manag. **264**, 115762 (2022). https://doi.org/10.1016/j.enconman.2022.115762

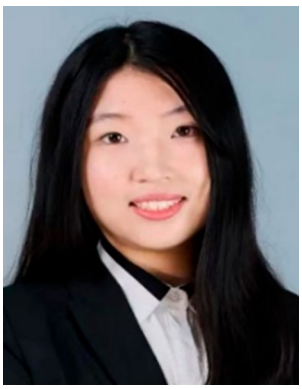

Chen-Ge Chen received her B.E. degree in Energy and Power Engineering from the East China University of Science and Technology in 2023. She is currently a Ph.D. candidate under the supervision of Prof. Yanwei Zhang and Prof. Chenyu Xu at the State Key Laboratory of Clean Energy Utilization, Zhejiang University. Her research interests focus on solid oxide electrolysis cells based on solar energy.

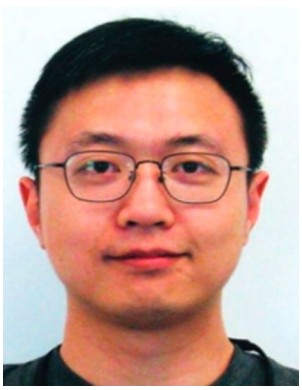

Chenyu Xu is a professor of the College of Energy Engineering at Zhejiang University. He received his Ph.D. degree in Energy and Environmental Engineering from Zhejiang University in 2018. His research focuses on hydrogen production and CO_2 conversion by both photothermal and photoelectric methods based on the utilization of solar energy.

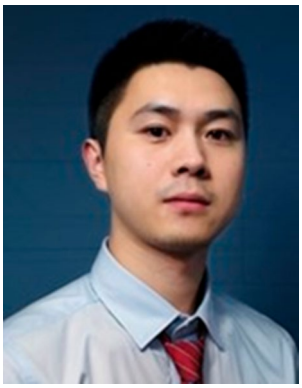

Peng-Fei Sui received his Ph.D. degree in Materials Engineering from the University of Alberta in 2023 and now works as a postdoctoral fellow at the University of Alberta. His research interests include developing nanomaterials and utilizing advanced characterization methods in the field of energy storage and conversion, mainly focusing on the electrochemical reduction of CO_2 and designing efficient catalysts and energy conversion systems.

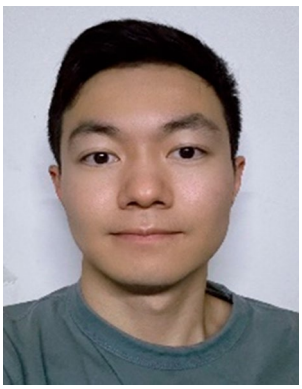

Guangyu Deng received his B.E. degree in Energy and Environmental Systems Engineering from Zhejiang University in 2018. He is currently a Ph.D. candidate under the supervision of Prof. Yanwei Zhang at the State Key Laboratory of Clean Energy Utilization, Zhejiang University. His research interests focus on solid oxide electrolysis cell based on solar energy.

Yi-Cheng Wang received his M.S. degree from the University of Calgary in 2021. Currently, he is a Ph.D. Candidate in the Department of Chemical and Materials Engineering at the University of Alberta. His research focuses on the cathode materials design for photoelectrochemical reduction of CO_2.

Jinhao Mei received his B.E. degree in Energy and Environmental Systems Engineering from Zhejiang University in 2022. He is currently a Ph.D. candidate under the supervision of Prof. Yanwei Zhang and Prof. Chenyu Xu at the State Key Laboratory of Clean Energy Utilization, Zhejiang University. His research interests focus on solid oxide electrolysis cells based on solar energy.

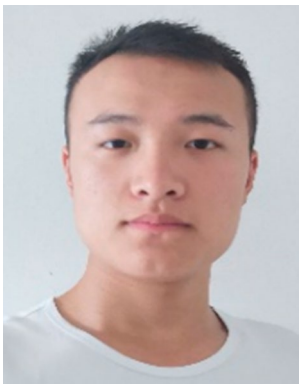

Entao Zhang received his B.E. degree in the College of Mechanical and Transportation Engineering from the China University of Petroleum (Beijing) in 2022. He is currently a Ph.D. candidate under the supervision of Prof. Yanwei Zhang and Prof. Chenyu Xu at the State Key Laboratory of Clean Energy Utilization, Zhejiang University. His research interests focus on the ordered full-spectrum conversion of solar energy.

Yanwei Zhang is a professor of the College of Energy Engineering at Zhejiang University. He received his Ph.D. degree in Engineering Thermophysics from Zhejiang University in 2008. His research interests include the photothermal synergistic synthesis of solar fuels, the full-spectral cascade utilization of solar energy, the design and application of advanced energy materials, first-principle quantum–mechanical calculation, and molecular dynamics calculation.

Jing-Li Luo is a Fellow of the Canadian Academy of Engineering and a professor emeritus in the Department of Chemical and Materials Engineering, the University of Alberta, Canada. She obtained her Ph.D. degree in Materials Science and Engineering at McMaster University, Canada, in 1992. Her current research has focused on fuel cells for natural resource conversion, energy storage materials, clean energy technology and corrosion control.